Rock Mechanics and Rock Engineering (2023) 56:3451–3474
https://doi.org/10.1007/s00603-023-03259-6

ORIGINAL PAPER

Effect of CO_2-H_2O-Smectite Interactions on Permeability of Clay-Rich Rocks Under CO_2 Storage Conditions

M. Zhang[1,2] · C. J. Spiers[2] · S. J. T. Hangx[2]

Received: 28 March 2022 / Accepted: 2 February 2023 / Published online: 23 February 2023

Abstract

CO_2 uptake by smectites can cause swelling and self-stressing in shallow clay-rich caprocks under CO_2 storage P–T and constrained conditions. However, little data exist to constrain the magnitude of the effects of CO_2-H_2O-smectite interactions on the sealing properties of clay-rich caprocks and faults. We performed permeability experiments on intact and fractured Opalinus Claystone (OPA) cores (~5% smectite), as well as on a simulated gouge-filled faults consisting of Na-SWy-1 montmorillonite, under radially constrained conditions simulating "open" transport pathways (dry and variably wet He or CO_2; 10 MPa fluid pressure; 40 °C). Overall, the flow of dry CO_2 through intact OPA samples and simulated smectite fault gouge caused a decrease in permeability by a factor of 4–9 or even by > 1 order, compared to dry He permeability. Subsequent to flow of dry and partially wet fluid, both fractured OPA and simulated gouge showed a permeability reduction of up to 3 orders of magnitude once flow-through with wet CO_2 was performed. This permeability change appeared reversible upon re-establishing dry CO_2 flow, suggesting fracture permeability was dominated by water uptake or loss from the smectite clay, with CO_2-water-smectite interactions play a minor effect. Our results show that whether an increases or decreases in permeability of clayey caprock is expected with continuous flow of CO_2-rich fluid depends on the initial water activity in the clay material versus the water activity in the CO_2 bearing fluid. This has important implications for assessing the self-sealing potential of fractured and faulted clay-rich caprocks.

Highlights

- Permeability of potential clay-rich caprock (Opalinus Claystone) was systematically measured using variably wet CO_2 versus He.
- Through-flow of dry CO_2 caused a decrease in permeability of intact Opalinus Claystone and simulated smectite fault gouge by up to > 1 order, as composed to dry He.
- Fractured Opalinus Claystone and simulated gouge showed a permeability reduction of up to 3 orders of magnitude with through-flow of wet CO_2.
- Permeability decrease by through-flow of variably wet CO_2 appeared reversible upon re-establishing dry CO_2 flow.
- The initial water activity in the clay material versus the water activity in the CO_2 bearing fluid determines change in permeability upon CO_2 flushing.

Keywords Shale permeability · CO_2 storage · Clay swelling · CO_2-H_2O-smectite interactions

✉ M. Zhang
zmcumtb@qq.com

[1] State Key Laboratory of Earthquake Dynamics, Institute of Geology, China Earthquake Administration, Beijing, China

[2] HPT Laboratory, Faculty of Geosciences, Utrecht University, Avenue Princeton 4, 3584 CB Utrecht, The Netherlands

1 Introduction

Safe, long-term storage of CO_2 in geological formations largely relies on the sealing quality of impermeable strata (caprock) overlying the storage reservoir. (Gaus 2010; Kaldi et al. 2011). This applies not only to CO_2 storage in depleted hydrocarbon reservoirs and saline aquifers (Benson and Cole

2008; Kaldi et al. 2013; Miocic et al. 2016; Song and Zhang 2013), but also to storage strategies linked to CO_2-enhanced oil and gas recovery from tight reservoir systems (Melzer 2012; Middleton et al. 2015; White et al. 2003). To evaluate leakage risk via fractures and faults present in clay-rich caprocks, much research has been done on interactions between CO_2, water (brine) and caprock-forming minerals. (c.f. review by Aminu et al. 2017; Kaldi et al. 2011; Song and Zhang 2013). Interactions between CO_2, water and the smectite clay components of shallow clay-rich caprocks have received particular attention, due to the ability of smectites to take up (sorb) both water and CO_2 into their interlayer structure, and onto the surfaces of the clay platelets, causing swelling (e.g., Ferrage et al. 2005; Giesting et al. 2012a; Loring et al. 2014).

It has long been known that incorporation of water molecules into the smectite interlayer structure produces expansion of the interlayer d_{001} spacing, as characterized by XRD. Relative to the water free (0W) state, incorporation of 1, 2 and 3 water layers, referred to as the 1W, 2W and 3W hydration states, causes 25, 55 and ~ 90% expansion, respectively (Barshad 1955; Berend et al. 1995; Bishop et al. 1994; Cases et al. 1992, 1997; Ferrage et al. 2005, 2007b; Laird 1999). More recently, it has also been shown, using a variety of XRD and spectroscopic techniques, that dry (supercritical) CO_2 molecules can penetrate and adsorb within the interlayer structure of smectites containing incompletely filled 1W or 2W hydration layers (i.e., with < 1 or between 1 and 2 water layers filled), causing interlayer expansion by up to ~ 15% (Giesting et al. 2012a, 2012b; Ilton et al. 2012; Loring et al. 2014, 2012; Romanov 2013; Rother et al. 2013; Schaef et al. 2012, 2015). By contrast, exposure of smectite clays with initial hydration states > 2W to dry (supercritical) CO_2 causes H_2O loss from the interlayer and shrinkage in the [001] direction by up to ~ 10% (c.f. Giesting et al. 2012a; Schaef et al. 2012). Exposure to variably wet CO_2 accordingly causes either interlayer swelling or shrinkage, depending on the partitioning of water and CO_2 molecules within the interlayer structure, which in turn must depend on their activities in the fluid phase and on the initial hydration state of the clay (Loring et al. 2014; Schaef et al. 2015).

Besides these XRD and spectroscopic studies, pre-pressed montmorillonite cubes (Na-SWy-1, hydration state < 1W) have been reported to exhibit volumetric swelling strains of 1–3% upon exposure to CO_2 at pressures up to 15 MPa at 45 °C (de Jong et al. 2014). Significant sorptive uptake of CO_2 by crushed, clay-bearing shales and SWy-1 and SAz-1 montmorillonites has also been documented under repository pressure and temperature conditions, falling in the range of 0.3–0.6 mmol/g and being accompanied by volumetric swelling strains of ~ 0.5% (Busch et al. 2008; Heller and Zoback 2014). It follows that CO_2 sorption is expected to cause swelling stress development under in-situ CO_2 storage conditions where free expansion is not possible. This was recently verified by Zhang et al. (2018), who measured 5–12 MPa axial swelling stress when pre-pressed montmorillonite discs were exposed to CO_2 at reservoir pressure and temperature conditions but with axial swelling strain restricted to ~ 1–3%. When swelling was totally restricted, the swelling stress increased to several tens of MPa.

Extensive researches have been performed to improve understanding of the impacts of various fluid-rock reactions on the sealing efficiency/integrity of caprock under the context of geological carbon storage (Espinoza and Santamarina 2012; Kampman et al. 2014a, 2014b; Skurtveit et al. 2018). Most of such studies have focused on carbonate dissolution/precipitation reactions and their effects on reactive permeability evolution (Armitage et al. 2013; Kampman et al. 2014a; Wollenweber et al. 2010; Wolterbeek et al. 2013). It is commonly observed that rock-fluid interactions (e.g., dissolution of formation rock and caprock, precipitation of secondary mineral phases) occurring in CO_2 storage system can lead to changes in pore structure and alternation of flow pathway, which in turn affects the transport properties of the reservoir and caprock (Rochelle et al. 2004; Skurtveit et al. 2018). However, possible alternation in transport properties within smectite-bearing clay-rich caprocks and fault gouges, induced by the experimentally confirmed swelling and shrinking of smectites due to CO_2 sorption, is poorly addressed in the literature (Skurtveit et al. 2018) except for a couple of modeling studies (Akono et al. 2019; Wentinck and Busch 2017). Moreover, most flow through experiments were conducted under controlled (effective) confining stress conditions (e.g., Gaus et al. 2005; Wollenweber et al. 2010), which are poorly representative for the near-zero lateral strain conditions encountered in the subsurface.

The present study experimentally addresses the effects of CO_2-H_2O interaction with smectite-bearing rock materials on permeability, under zero lateral strain boundary conditions. The intension is to provide constraints for evaluating the sealing integrity of clay-rich caprocks overlying CO_2 storage reservoirs, while pore fluid displacement sequences occur due to CO_2 injection (e.g., dry or wet CO_2 displacing host pore fluid) and penetration of leaking reservoir fluid into pore networks, fractures or faults in clay-rich caprocks (Kim and Hosseini 2014; Busch et al. 2016). Particularly, we focus on the behaviour of initially open transport paths in samples subjected to near-zero initial effective normal stress and constrained to zero lateral strain. We conducted multiple-run permeability measurements on cylindrical Opalinus Claystone (OPA) samples and on a simulated smectite fault gouge layer, constrained in a stainless vessel. All samples were first tested using dry He and dry CO_2, to distinguish the effect of CO_2-rock interactions from the poromechanical effect as characterized by control experiments using non-sorbing He. Subsequently, flow-through tests using wet He

and wet CO_2 were performed on one OPA sample and the simulated smectite gouge, aimed to reveal the impacts of interactions between CO_2, H_2O and the clay components. Our results show that stress–strain-sorption related changes in permeability amount up to 3 orders of magnitude.

2 Experimental Methods

We performed axial permeability measurements at 40 °C on two, radially constrained, cylindrical Opalinus Claystone samples (35 mm diameter × 70 mm length), one cored perpendicular and one cored parallel to the bedding plane. A third experiment was conducted on a simulated gouge layer made of Na-rich montmorillonite. Each sample was first subjected to multiple flow-through runs conducted using dry CO_2, and dry inert He as the flowing fluid. These were aimed at revealing the effects of dry CO_2 on permeability, independently of poroelastic effects as characterized by the tests using He. To better simulate multiple pore fluid displacement processes that might occur in a potential CO_2 storage system and to demonstrate the effect of interactions between water, CO_2 and swelling clay components on transport properties of (faulted) caprock, the OPA sample cored parallel to bedding was subsequently fractured and subjected to similar measurements as well as extra experimental runs using wet He, wet CO_2, pure liquid water, CO_2-saturated water, water-saturated CO_2, water-saturated He, dry CO_2 and dry He. These additional tests were performed only on the parallel-to-bedding OPA sample because changes in permeability associated with swelling/shrinking effects are expected to be more pronounced for such bedding orientation, since the swelling/shrinking effects caused by sorption in OPA mudstone are much greater in the direction perpendicular to the layer than parallel to the layer (Thury 2002). The simulated gouge sample was subjected to alternative runs using dry (pure) versus wet CO_2 after initial testing with dry CO_2 and dry He, aimed to further verify the effects of water activity on the permeability change associated with CO_2-smectite interaction.

2.1 Starting Material and Pore Fluids

The Opalinus samples used here were derived from a block of the shaly facies of the Jurassic Opalinus Claystone (Bossart and Thury 2008; Thury 2002). The block was extracted and provided by the Mont Terri Underground Rock Laboratory (Switzerland). The reference mineralogical composition of OPA material is illite 18%, kaolinite17%, mixed layer illite/smectite 10–14%, chlorite 5%, quartz 20%, calcite 16%, with trace amount of dolomite, feldspar and pyrite (Pearson et al. 2003; Thury 2002; Vinsot et al. 2017). The smectite starting material, used to make a simulated fault gouge layer, was sampled from a single batch of Na-rich Wyoming montmorillonite powder (Na-SWy-1), obtained from the Source Clays Repository of the Clay Minerals Society. The material was used in the as-received condition. Quantitative XRD analysis conducted at RWTH Aachen University showed that the batch was composed of 73% (Na-rich) smectite, 10% quartz, 6% muscovite/illite, 9% feldspar plus traces of carbonate and gypsum. Detailed characterization of the Na-SWy-1 clay can be found in Van Olphen and Fripiat (1979) and De Jong et al. (2014). The CO_2 and He used as (flowing) pore fluids were supplied at > 99.99% purity level by Air Products NL. Aqueous pore fluids were prepared using deionized water.

2.2 Experimental Methods and Procedures

2.2.1 Sample Preparation

The two OPA claystone samples tested (Samples A and B) were cored from the claystone block, as received from the Mont Terri laboratory, using a diamond coring bit cooled with compressed air. Sample A was cored perpendicular to the bedding while Sample B was cored parallel to the bedding. The ends of the samples were ground flat and perpendicular to the cylindrical axis. The simulated Na-SWy-1 gouge sample was prepared by compacting ~ 14 g of Na-SWy-1 montmorillonite powder between two half-cylindrical stainless steel blocks (Fig. 1). To do so, the montmorillonite powder was first dried in lab air at 40 °C > 48 h, and then evenly distributed on the flat face of the lower half cylinder, supported in a dedicated steel base. The upper half cylindrical block was subsequently located to sandwich the clay layer as shown in Fig. 1. The sandwiched clay layer and enclosing half cylindrical blocks thus formed a fully cylindrical assembly that was clamped together using two bolts

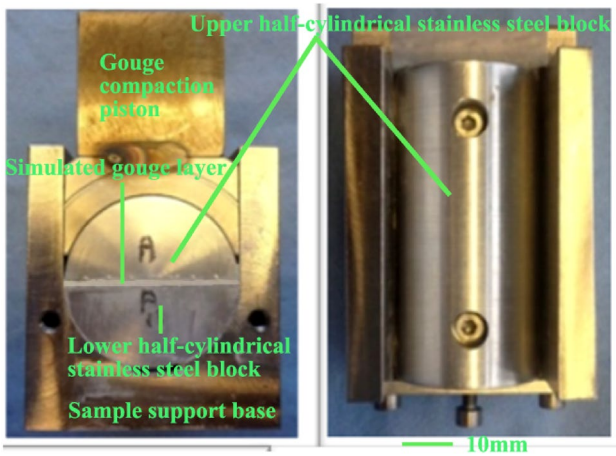

Fig. 1 Set-up used for preparation of the simulated smectite gouge assembly

penetrating the steel blocks. The sample assembly was then loaded normal to the simulated fault plane, using a specially designed holding piston (Fig. 1) at 60 MPa and at lab temperature and humidity, for a total of 12 h. The compaction process was temporarily stopped every ~ 3 h, removing the load, tightening the bolts and then applying the load again, which finally yielded a cylindrical sample assembly with an axially aligned, normally loaded smectite layer around a 0.8 mm thick. Basic data of the samples tested are listed in Table 1.

2.2.2 Sample Confinement for Axial Permeametry at Zero Radial Strain

Each sample was constrained to near zero radial displacement at the outer cylindrical boundary by gluing it into a closely fitting, individually made, stainless steel pressure vessel (inner diameter = 35.2 mm, length = 70 mm, outer diameter = 45 mm, i.e., wall thickness s = 4.9 mm). To achieve this, each sample was pushed into its pressure vessel (see Fig. 2) with the gap between the sample and inner vessel wall (1.0–1.5 mm) being filled by a thin layer of Argomet epoxy resin (strength > 100 MPa). The sample plus vessel was left undisturbed in heated lab air at ~ 40 °C for approximately one week, to allow curing. This procedure also allowed the sample to equilibrate with the lab air relative humidity (RH≈20% at 40 °C), the smectite present in the sample thus was estimated to achieve a hydration state of H < 1W for Na-rich type and 1W < H < 2W for Ca-rich type, following Ferrage et al. (2007a) and Morodome and Kawamura (2009). Threaded stainless steel closure caps, with external flow connections and internal flow distributors (porous stainless steel plates), were subsequently screwed onto the ends of each sample vessel, sealing against the vessel using two Viton O-rings located in circular grooves at the vessel ends (Fig. 2b–e). The sample/vessel assembly was then ready for connection to the permeameter system.

2.2.3 Permeametry Set-up and Conditions

Flow-through experiments were performed in a purpose-built permeameter system (Fig. 2f) capable of running at a temperature of 20–60 °C (± 0.2 °C) and fluid pressures up to 20 MPa, thus approaching shallow reservoir conditions. The setup consists of two Teledyne ISCO syringe pumps (model 65D, capacity = 67 mL, 0.7–1390 bar) connected to the up- and downstream ends of the glued sample/vessel assembly (Fig. 2c–-e). The pumps, controlled using LabView-based software, are capable of running in constant pressure, constant volume or constant flow rate mode. The high pressure tubing and value system is arranged such that the pumps and sample can be independently evacuated and/or charged with deionized water, He (gas bottle) or CO_2 (gas bottle) (Fig. 2f). During individual experiments, the glued sample/vessel assembly is immersed in a water bath, with the water temperature being measured using a Pt-100 resistance element and controlled by an integrated immersion heater and circulator pump. The same pump circulates hot water at controlled experimental temperature through heating jackets installed on the syringe pump cylinders. The entire system is enclosed in a polystyrene box to further stabilize the air temperature around the set-up. Temperature inside the box is measured using a Pt100-element and kept constant at 40° C by means of a 500 W light bulb connected to a digital CAL9000 PID-controller. The air temperature inside the box is homogenized by circulating the air using two powerful fans operating at constant speed. In the present flow-through experiments, a PC equipped with LabView-based software was used to log all temperature, pump volume, flow-rate and pressure signals, at intervals of 5 s.

Table 1 Basic data on samples investigated in the present permeability experiments

Sample ID	Sample material	Sample orientation	Mass g	Length mm	Cross section mm^2	Density g/cm^3	Porosity %
A	OPA	Perpendicular	152.16	68.5	961.6	2.31	13.4 ± 1.2[a]
B	OPA	Parallel	157.48	69.1	961.6	2.37	16.6 ± 1.1[a]
C	Na-SWy-1	Parallel	4.60	69.58	25[b]	2.36	22[b]

Orientation defines the bedding/ fabric orientation relative to the longitudinal sample axis, i.e., the direction of imposed fluid flow. Cross section refers to sample cross section measured normal to fluid flow. Mass and density values were measured before each sample was glued in to the pressure vessel

[a]Porosity values for OPA Samples A and B were obtained from the excess He volume pumped into the pore fluid system plus sample, relative to the volume of the system with a stainless steel dummy sample present. The error given is associated with uncertainly in the measurement of tube volumes

[b]The porosity of the simulated gouge was estimated from the mass, dimensions and hence density of the pre-pressed sample versus the referential dry density of the SWy-1 montmorillonite (~ 2.3 g/cm^3 at hydration state ≤ 1W, from the database of the Clay Minerals Society)

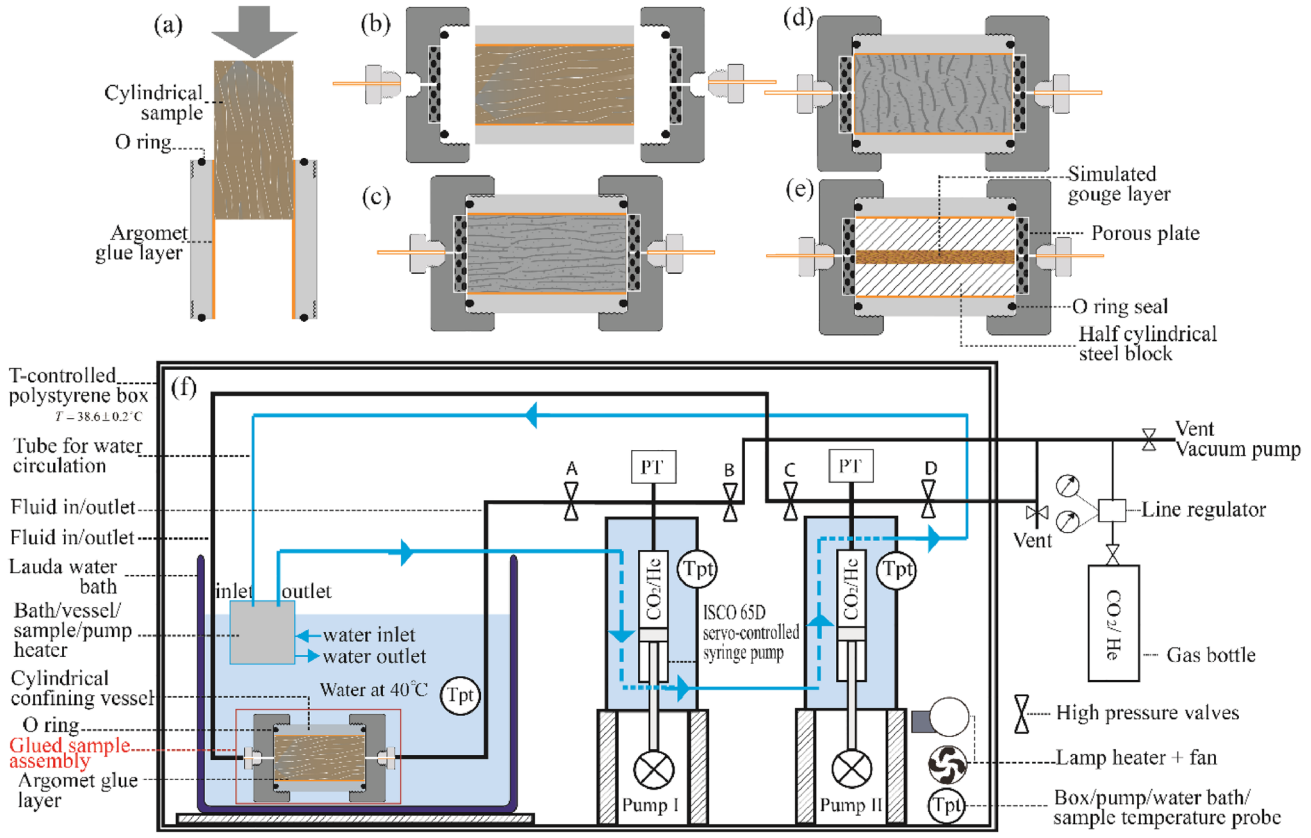

Fig. 2 Semi-schematic diagram illustrating sample assembly and experimental setup. **a** Cylindrical sample being inserted and glued into the stainless steel vessel. **b** Components of each sample assembly. **c** Sample/vessel assembly for OPA Claystone Sample B cored parallel to bedding **d** Sample/vessel assembly for OPA Claystone Sample A cored perpendicular to bedding. **e** Sample assembly containing simulated smectite gouge, constrained between two half-cylindrical steel blocks. All samples are laterally constrained by the enclosing vessel to simulate conditions of zero lateral strain. **f** Schematic representation of the permeameter set-up

2.2.4 Permeametry Procedure

The flow-through experiments and permeametry were performed using the steady state method. After installing the sample/vessel assembl

y in the water bath, the system was heated to the experimental temperature of 40 °C. The two ISCO syringe pumps were then primed with the desired pore gas/fluid (initially He, Series 1), independently of the rest of the system. The sample assembly was subsequently degassed for ~ 2–4 h by applying a vacuum. Following Morodome and Kawamura (2009) and since the water loss kinetics from smectites is slow, the hydration state of smectite after degassing is assumed to be unchanged compared with that attained after equilibration with lab air humidity at 40 °C (i.e., H < 1W for Na- and 1W < H < 2W for Ca-rich smectite). We refer to this hydration state henceforth as the "initial hydration state". Following this degassing procedure, the sample-pump system was uniformly pressurized with the pore fluid phase (initially He, Series 1) to 10 MPa, with the upstream (US) pump almost fully filled and the downstream (DS) pump near-empty. After equilibration for a duration of few minutes to several tens hours (see Table 2), the through flow run was initiated by applying $\frac{1}{2}\Delta P$ increment to the US pump pressure and $\frac{1}{2}\Delta P$ decrement to the DS pump pressure, hence a target differential pressure equal to ΔP was applied across the sample. Both pumps were subsequently run in constant pressure mode, so that a mean flowing fluid pressure of 10 MPa and a constant differential pressure of ΔP were maintained across the sample. The magnitude of the resulting flow of fluid from the US to the DS pump, recorded by the volume change of both pumps, provided a measure of sample permeability at steady state (constant, equal but opposite flow rates at each pump). The same procedure was followed for all fluids used, but the degassing procedure using vacuum lasted only a few minutes except for Series 1 measurements. Fluid flow and permeability measurement were performed continuously (by steady state method, see details in Appendix 1), except when suspended intermittently in the following situations, which produced transient effects: (a) When the pumps needed restroking or recharging due to slow leakage (fluid pressure in sample

Table 2 Experimental conditions and key results of permeability experiments done in present study

Sample/ Serial NO	Flowing fluid	Run NO	Elapsed time to run start (hour)	Flow duration (min/hour)	P_I (0.1 MPa)	P_II (0.1 MPa)	ΔP (*0.1 MPa)	Pem.I (m^2)	Pem.II (m^2)
Sample A									
Series 1	Dry He	Run 1	0.33	41.6 h	100.25	102.06	–1.86	2.5E-18	3.3E-18
Series 2	Dry CO_2	Run 1	24.5	196.5 h	100.24	102.07	–1.89	6.34E-19	7.92E-19
Series 2	Dry CO_2	Run 2	290.52	105 h	100.27	102.04	–1.88	1.2E-18	1.7E-18
Sample B (intact)									
Series 1	Dry He	Run 1	0.5	3.5 min	99.99	99.15	0.73	4.9E-15	4.9E-15
Series 1	Dry He	Run 2	0.67	3.75 min	100.12	100.45	–0.47	5.2E-15	5.1E-15
Series 1	Dry He	Run 3	0.83	4.24 min	99.74	100.20	–0.56	4.5E-15	4.5E-15
Series 1	Dry He	Run 4	3	10 min	100.15	99.69	0.29	4.5E-15	4.5E-15
Series 1	Dry He	Run 5	4.17	3.4 min	99.75	100.21	–0.61	5.2E-15	5.2E-15
Series 2	Dry CO_2	Run 1	2.00	53 min	99.61	100.31	–0.93	5.7E-16	5.5E-16
Series 2	Dry CO_2	Run 2	4.64	80 min	100.49	99.50	0.83	5.0E-16	4.9E-16
Series 2	Dry CO_2	Run 3	9.48	66.7 min	99.53	100.51	–1.21	4.2E-16	4.1E-16
Series 2	Dry CO_2	Run 4	24.14	110 min	100.49	99.65	0.74	4.1E-16	4.1E-16
Series 2	Dry CO_2	Run 5	52.15	75 min	99.53	100.51	–1.10	4.2E-16	4.1E-16
Series 2	Dry CO_2	Run 6	55.58	68 min	100.48	99.50	0.89	4.1E-16	4.0E-16
Series 3	Dry He	Run 1	0.07	4.6 min	100.08	99.94	0.14	1.8E-14	1.8E-14
Series 3	Dry He	Run 2	1.7	3 min	100.30	100.18	–0.14	1.8E-14	1.7E-14
Series 3	Dry He	Run 3	5.1	4.1 min	99.97	100.10	–0.13	2.1E-14	2.1E-14
Series 3	Dry He	Run 4	16.4	2.3 min	99.96	100.25	–0.09	1.5E-14	1.5E-14
Series 3	Dry He	Run 5	17.6	2.1 min	100.46	100.64	–0.10	2.5E-14	2.5E-14
Series 4	Dry CO_2	Run 1	0.17	5 min	99.81	100.29	–0.66	4.4E-15	4.3E-15
Series 4	Dry CO_2	Run 2	2.33	22 min	100.17	99.73	0.43	2.7E-15	2.7E-15
Series 4	Dry CO_2	Run 3	3	13 min	99.70	100.18	–0.50	3.3E-15	3.2E-15
Series 4	Dry CO_2	Run 4	32	28.3 min	100.47	99.50	0.63	1.9E-15	1.9E-15
Series 4	Dry CO_2	Run 5	33	14.1 min	99.51	100.49	–0.97	2.2E-15	2.2E-15
Series 4	Dry CO_2	Run 6	173	9 min	99.06	100.02	–1.28	2.2E-15	2.1E-15
Sample B (fractured)									
Series 5	H_2O-saturated He	10 runs	NR	NR	99–101	99–101	0.5–2	*	*
Series 6	H_2O-saturated CO_2	16 runs	NR	NR	99–101	99–101	~2	*	*
Series 7	H_2O	1 run	NR	NR	109.60	90.13	19.87	*	*
Series 8	CO_2-saturated H_2O	1 run	NR	NR	109.89	90.07	19.79	*	*
Series 9	H_2O-saturated CO_2	2 runs	NR	NR	105.21	95.12	10.14	*	*
Series 10	H_2O-saturated He	1 run	NR	NR	101.74	98.69	3.10	*	*
Series 11a	Dry CO_2	44 runs	NR	NR	99–101	99–101	0.13–2	*	*
Sample C									
Series 1	Dry He	Run 1	0.1	5.4 min	99.61	100.31	–0.93	4.7E-14	5.1E-14
Series 1	Dry He	Run 2	1.5	6.3 min	100.49	99.50	0.83	5.0E-14	4.9E-14
Series 2	Dry CO_2	Run 1	10	15 min	100.56	100.01	–0.40	9.8E-15	9.5E-15
Series 2	Dry CO_2	Run 2	35	74.2 min	99.02	100.00	–1.94	7.8E-15	7.7E-15
Series 2	Dry CO_2	Run 3	145	67.5 min	101.98	99.02	1.86	7.5E-15	7.7E-15
Series 2	Dry CO_2	Run 4	255	70.5 min	99.71	100.97	–2.28	6.3E-15	6.5E-15
Series 2	Dry CO_2	Run 5	425	50 min	101.98	99.02	1.92	7.3E-15	7.5E-15
Series 2	Dry CO_2	Run 6	540	15 min	100.03	101.00	–1.99	7.2E-15	7.2E-15
Series 2	Dry CO_2	Run 7	1440	60 min	101.05	99.14	2.11	6.8E-15	6.7E-15
Series 3	CO_2(100%H_2O saturated)	Run 1/8	160	68	99.10	101.99	–1.90		

Table 2 (continued)

Sample/ Serial NO	Flowing fluid	Run NO	Elapsed time to run start (hour)	Flow duration (min/hour)	P_I (0.1 MPa)	P_II (0.1 MPa)	ΔP (*0.1 MPa)	Pem.I (m^2)	Pem.II (m^2)
Series 3	CO_2(100%H_2O saturated)	Run 2/9	815	432	99.40	102.00	–1.48		
Series 3	CO_2(25%H_2O saturated)	Run 3/10	1295	1300	101.01	100.33	1.76	2.8E-16	5.2E-16
Series 3	CO_2(100%H_2O saturated)	Run 4/11	300	2800	99.19	102.06	–1.40		
Series 3	Dry CO_2	Run 5/12	60	14,000	98.20	102.11	–4.65		
Series 3	CO_2(80%H_2O saturated)	Run 6/13	1300	1320	101.50	99.34	2.60	4.5E-16	1.3E-16
Series 3	Dry CO_2	Run 7/14	200	1724	99.36	102.00	–2.52	1.2E-16	1.1E-15
Series 3	CO_2(100%H_2O saturated)	Run 8/15	430	780	101.98	98.92	3.31		

All experimental/series runs were performed at 40 °C, with a mean pore fluid pressure of 10 MPa otherwise stated

Elapsed time is the time elapsed since the start of any series of runs performed using the same pore fluid, (i.e., since the moment a given pore fluid was introduced into the sample)

P_I and P_II are the mean pressure values recorded by pumps I and II during each flow-through run. ΔP is the mean differential pressure applied across the sample during each run. Perm I and Perm II are the mean permeabilities for an individual run, obtained from the volume versus time data of Pumps and I and II, respectively

*Multiple data reported in Figures only. NR represents multiple runs that time data not reported here

maintained at 10 MPa); (b) When changing fluids, e.g., from He to CO_2 or from CO_2 to water, in one or both pumps. When using dry He and/or CO_2, restroking was achieved by reversing the differential pressure and flow direction, except where stated otherwise. Changing from one fluid to the next was done by with briefly evacuating the pore fluid system plus sample and then injecting the new pore fluid from the upstream pump-tubing system. We refer to any unbroken flow-through measurement, with one fluid in one direction, as one "run". The permeability evolution within each run was determined assuming flow involved a series of steady states. Testing "series" employing the same flowing fluid consisted of one or more sequential runs separated by pump restroking or pump recharging, aimed at obtaining a constant (apparent) permeability, (i.e., no discernible change with further through-flow), indicating equilibrium between sample and fluid.

In the present study, all three sample assemblies were first tested using dry (pure) He and then dry (pure) CO_2 as the flowing fluid. These run sequences using He and CO_2 are denoted as Series 1 and Series 2 measurements, respectively (See Table 2). In the case of Sample A (OPA sample cored perpendicular to bedding), Series 1 consisted only one flow-through run, performed using dry He at a differential pressure ΔP of 0.2 MPa applied 20 min after the initial introduction of He at 10 MPa. In the Series 2 experiments on Sample A, 2 runs were performed using dry CO_2, starting at a total elapsed time of 24.5 and 290.52 h after CO_2 introduction.

In the case of Sample B (OPA sample cored parallel to bedding), 5 dry He runs (Series 1) and then 6 dry CO_2 runs (Series 2) were performed on the intact sample in similar way to Sample A (Table 2). The procedure was then repeated in a second cycle again using dry He first (Series 3, 5 runs) and then dry CO_2 (Series 4, 6 runs). In a deliberate attempt to fracture the sample inside its vessel, the sample assembly was then disconnected from the permeameter system and Sample B subjected to several cycles of dehydration and rehydration at ~ 45 °C, achieved by exposing it to heated lab air (RH≈16% at 45 °C) and air buffered using saturated NaCl solution (RH≈75% at 45 °C). This cycling ultimately produced two bedding-parallel fractures in the sample following equilibration with ~ 75% relative humidity. The thus fractured sample was then tested sequentially using water-saturated He (Series 5), water-saturated CO_2 (Series 6), liquid water (Series 7), CO_2-saturated water (Series 8), water-saturated CO_2 (Series 9), water-saturated He (Series 10) and dry CO_2 (Series 11a). Each of these series included one to several tens of sequential runs, aimed at obtaining a stable apparent permeability assumed to represent equilibrium between with the sample and pore fluid. During the break between sequential runs, the sample was exposed to the pore fluid pressure at 10 MPa (ΔP = 0) for a duration of several minutes to several tens of hours. See Table 2 for detailed experimental conditions.

As for the simulated smectite gouge sample (Sample C), after testing using dry He (Series 1) and dry CO_2 (Series 2),

several tests were sequentially conducted in a multi-fluid series (Series 3) employing dry CO_2, water-saturated CO_2, water-undersaturated CO_2 and again dry CO_2. These runs were attempted to discriminate between effects of dry and wet CO_2.

Water-saturated CO_2 employed in the first run of the multi-fluid Series 3 experiments performed on Sample C, was created by adding ~ 5 mL deionized water to the US pump, then pressurizing the US pump with CO_2 via a diaphragm pump, until the CO_2 pressure reached 10 MPa. The US pump was subsequently isolated from the gas supply system and maintained at the desired US pressure in pressure control mode. When the fluid volume in the US pump became stable (i.e., when the CO_2-water system reached equilibrium), flow through was initiated by opening the connections between sample assembly and both pumps. Except for the first run, all water-saturated CO_2 and CO_2-saturated water and water saturated He fluids used in the present study were prepared in a reaction vessel (see detail in Wolterbeek et al. 2016) allowing for sufficient mixing of CO_2 and water or He and water at 10 MPa and 40 °C. Undersaturated water-bearing CO_2 was obtained by mixing water-saturated CO_2 with dry CO_2 in a controlled volumetric ratio (e.g., mixing water-saturated CO_2 and dry CO_2 at a 4:1 volumetric ratio produced CO_2 with 80% water saturation).

2.2.5 Calibrations and Data Processing

Prior to any flow-through test, leakage rate of the flow-through system with respect to each flowing fluid was measured with a stainless steel dummy sample connected to the permeatry system, which allows for flow-rate across a real sample to be accurately obtained after correcting for the leakage. Meanwhile, the upstream and downstream tube volumes were measured (see Appendix A1.1). Permeability of the sample measured in individual test was calculated from the corrected flow rate using Darcy's law, detailed description of the calculation process was presented in Appendix A1.2.

2.3 XRD and Infrared Analysis of Sample Material

XRD diffraction measurements were performed on the starting materials and on samples after permeability testing, using an X-ray diffractometer (Rigaku D/max-rB) equipped with a Cu- K-alpha X-ray source, to asses if any mineralogical changes occurred due to fluid through-flow, e.g., flow of $ScCO_2$. In the case of the OPA clay, cuttings collected during coring and preparation were crushed using a pestle and mortar and used to represent the starting material. The as-received Na-SWy-1 clay was used directly for XRD analysis of the starting smectite gouge. After termination of the experiments on each sample (i.e., Samples A, B and C), a small portion of sample material was retrieved from one end and similarly powered using a pestle and mortar for XRD testing. Quantitative phase analysis was done using the XRD profiles collected for each sample. In addition, Fourier-transform infrared spectroscopy (FTIR) measurements were performed on the Na-SWy-1 starting material and on samples retrieved from the simulated Na-SWy-1 gouge sample after experimentation.

Before the commencement and after termination of experiments on each sample, when the samples were accessible for visual observation, the end surfaces were visually examined and photographed to record any changes in the surface morphology.

3 Results

3.1 Flow-Through Data

The specific experimental sequence, the experimental conditions and key data for all runs performed on the three samples investigated are tabulated in Table 2.

3.1.1 Flow-Through and Apparent Permeability Data for Sample A

The results of the permeability measurements performed on OPA Sample A (flow normal to bedding) using pure (dry) He (Series 1, 1 run) and then pure (dry) CO_2 (Series 2, 2 runs) as flowing fluid are presented in terms of flow and measured (apparent) permeability versus time in Fig. 3. Here, time refers to elapsed time since each pore fluid was introduced into the sample at 10 MPa. Figure 3 shows that the permeability of Sample A measured perpendicular to bedding lies at around $1.3 \times 10^{-18} m^2$ for He, with little or no change occurring with time. By contrast, the CO_2 permeability measured in Series 2/Run 1 is ~ $7 \times 10^{-19} m^2$, corresponding to a steady through-flow of ~ 30 mL CO_2 over ~ 200 h. The CO_2 permeability then measured in Run 2 increases from ~ $1.1 \times 10^{-18} m^2$ to ~ $1.8 \times 10^{-18} m^2$ and then stabilizes at the latter value with flow of ~ 33 mL CO_2.

3.1.2 Apparent Permeability Data for Sample B

3.1.2.1 Intact Sample Data The measured (apparent) permeability versus time data for intact OPA Sample B (parallel to bedding), measured in the Series 1–4 runs performed sequentially using dry He, dry CO_2, dry He and dry CO_2, are plotted in Fig. 4 and listed in Table 2. The Series 1 (He) data are presented in Fig. 4a. This shows the average He permeability coefficients measured in each of the 5 runs of Series 1, as a function of elapsed experimental time since introducing He at 10 MPa. The five individual runs, starting when

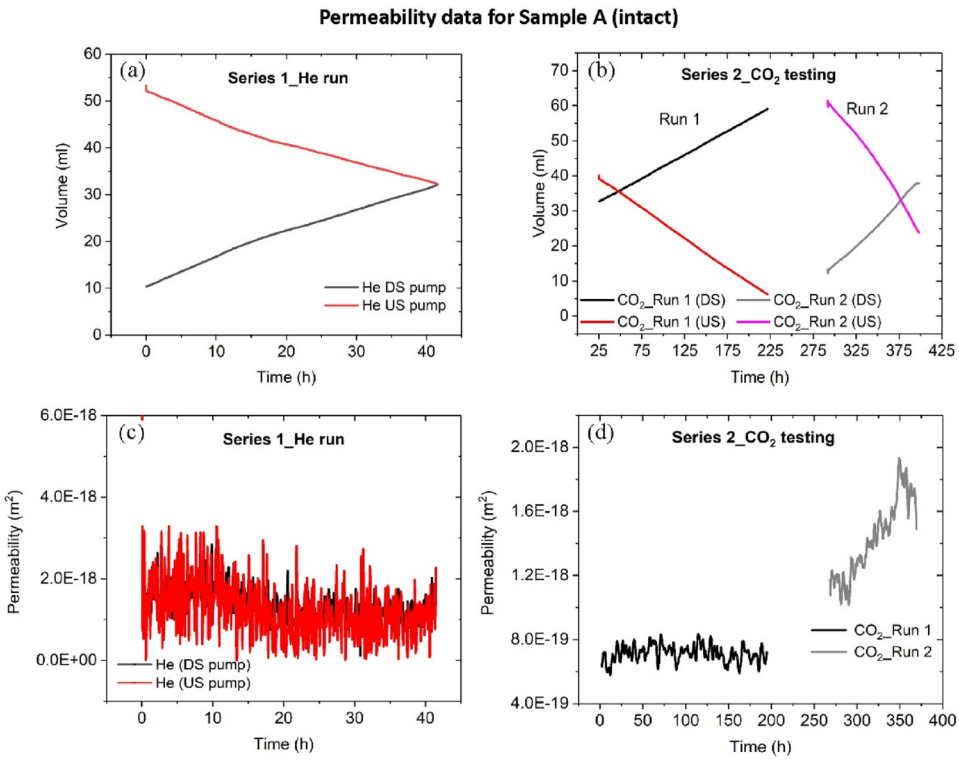

Fig. 3 Flow and permeability data for intact Sample A measured normal to bedding. **a** Flow of He versus time. **b** Flow of CO_2 versus time. **c** He permeability versus time. **d** CO_2 permeability versus time. Zero time is the moment at which a given pore fluid pressure was introduced into the sample at 10 MPa pressure. Hence, time here refers to the total duration that the sample was exposed to each pore fluid. It also gives indication of the starting time and duration of each experimental run. Note: Time gaps between Run 1 and 2 in **b** and **d** represents pump recharging interval during which the sample was exposed to pore fluid pressure at 10 MPa but without through flow

the sample had been exposed to He pressure for 0.5–4.2 h with each run lasting for 3–5 min (see Table 2), exhibit similar values of apparent permeability ($4.5–5.3\times10^{-15}m^2$), and show no dependence on time.

The Series 2 measurements, performed on intact OPA Sample B using pure (dry) CO_2, consist of 6 individual runs (Table 2). The permeability versus elapsed time data for the first and last runs are plotted in Fig. 4b, c to illustrate typical results. The mean permeability values obtained at the start and end of Run 1 and in each of Runs 2–5 are plotted versus elapsed time since CO_2 introduction in Fig. 4d. All He permeability values measured in Series 1 are lower than obtained for CO_2 in Series 2. Figure 4b–d show that, during the first 10 h of exposure to and through-flow of CO_2, sample permeability decreased by about 40% from ~ 7×10^{-16} to ~ $4\times10^{-16}m^2$, then stabilizing at this value, which is ~ one order lower than that measured using dry Helium (Fig. 4a). The subsequent Series 3 permeability measurements performed on intact OPA Sample B (using dry He) are shown in Fig. 4e. These show a clear increase in permeability from the final Series 2 value of $4\times10^{-16}m^2$ obtained using CO_2, to values around $2\times10^{-14}m^2$. Switching back to dry CO_2 in the Series 4 measurements produced a decrease again to a stable value of ~ $2\times10^{-15}m^2$ within about 10 h (Fig. 4f).

3.1.2.2 Fractured Sample Data The bedding-parallel permeability results obtained Sample B after desiccation fracturing, in the Series 5 to 11 permeability runs, are shown in Fig. 5a–h. Recall that these series were performed sequentially using H_2O-saturated He (Series 5), H_2O-saturated CO_2 (Series 6), Liquid H_2O (Series 7), CO_2-saturated H_2O (Series 8), H_2O-saturated CO_2 (Series 9), H_2O-saturated He (Series 10), and finally dry CO_2 (Series 11), all at a mean fluid pressure of 10 MPa (see Table 2), are presented in Fig. 5a–h.

In the Series 5 runs using H_2O-saturated He, the apparent permeability of fractured Sample B (pre-equilibrated with 75% RH) fell rapidly from 8.6×10^{-14} to 5.8×10^{-15} m^2, stabilizing at the latter value beyond 20 h of exposure to the pore fluid (see Fig. 5a). The apparent permeability was further reduced by flow of H_2O-saturated CO_2 in the Series 6 runs, decreasing swiftly to 3×10^{-15} m^2 in ~ 3 h and gradually reaching a steady value of 2.8×10^{-15} m^2 at ~ 20 h (Fig. 5b). Subsequently, using water at 10 MPa mean pressure as the flowing fluid (Series 4), the permeability decreased sharply. Almost no flow was measured by the downstream (DS) pump over ~ 5 h under an initially applied differential pressure of 0.4 MPa (Fig. 5c), and this remained so until the differential pressure was increased to 2 MPa (Fig. 5c), presumably when the breakthrough pressure was achieved. The apparent permeability then measured using water was ~ $2\times10^{-19}m^2$, exhibiting negligible change over 60 h of through-flow (Fig. 5d). Establishing a continuous flow of CO_2-saturated H_2O thereafter, i.e., in the single Series 8 run, gradually increased the apparent permeability from ~ 5×10^{-19} m^2 to 2×10^{-18} m^2 over 100 h

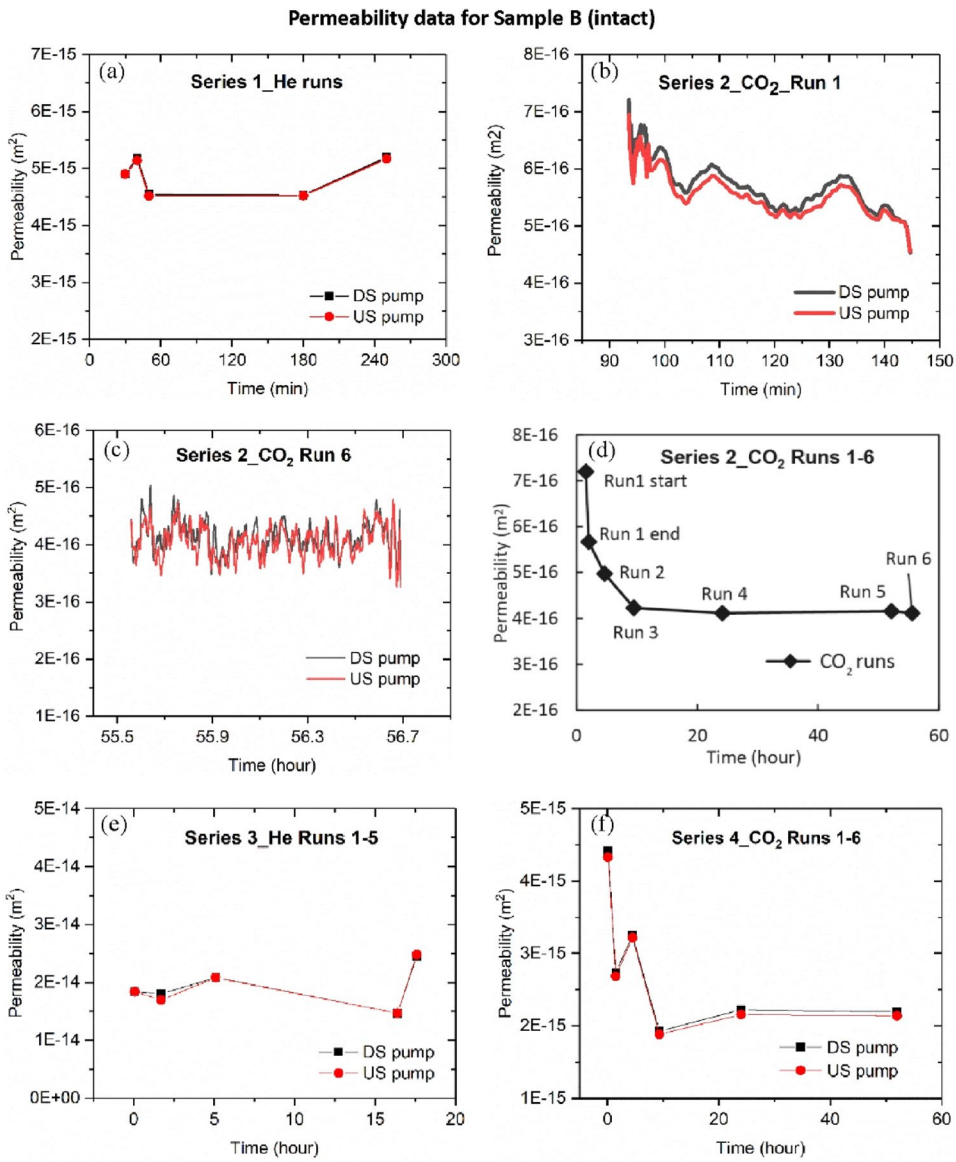

Fig. 4 Permeability versus time measured in the Series 1–4 experiments performed on intact Sample B (parallel-to-bedding). **a** Average permeabilities measured in Series 1 runs using dry He. **b** Permeability evolution in the first run of Series 2 measurements conducted using dry CO_2. **c** Permeability evolution in the last run of Series 2 conducted using dry CO_2. **d** CO_2 permeability change from the first to the last run of Series 2. **e** Permeability change throughout the Series 3 runs performed using dry He. **f** Permeability change throughout the Series 4 runs performed using dry CO_2

(Fig. 5e). Flow through of H_2O-saturated CO_2 (Series 9, 1 run) then increased the permeability further, reaching a new steady value of ~ 2.5×10^{-18} m^2 (Fig. 5f). Little change occurred when the fluid was subjected to H_2O-saturated He (S10, 1 run) over 40 h of flow (Fig. 5g). The permeability runs were then continued using dry CO_2 (Series 11a, 44 runs). No change from the wet CO_2 and wet He values of ~ 2.5×10^{-18} m^2 occurred in the first 120 h of dry CO_2 flow. However, beyond 150 h, the permeability increased rapidly reaching a near steady value of 5.9×10^{-13} m^2 after the sample had been exposed to the dry CO_2 for ~ 600 h (Fig. 5h). After a total of ~ 1600 h of dry CO_2 flow at 10 MPa mean pressure (Series 11a), the permeability reached a stable value at ~ 6×10^{-13} m^2.

3.1.3 Apparent Permeability Data for Sample C (Simulated Smectite Gouge)

The initial Series 1 permeability runs performed on Sample C using dry He (two runs), yielded similar permeability values of ~ 5×10^{-14} m^2 (see Table 2). The permeability results obtained for the subsequent Series 2 runs on Sample C, conducted using dry CO_2 (Runs 1–7) are presented in Fig. 6, as are the Series 3 data (Runs 1–8) obtained for alternating wet and dry CO_2 flow (refer Table 2). The permeability evolution shown by the Series 2 runs conducted with pure CO_2 (Runs 1–7) is plotted against elapsed (i.e., CO_2 exposure) time in Fig. 6a. This shows that the dry SWy-1 montmorillonite "gouge" layer experienced a small reduction in permeability

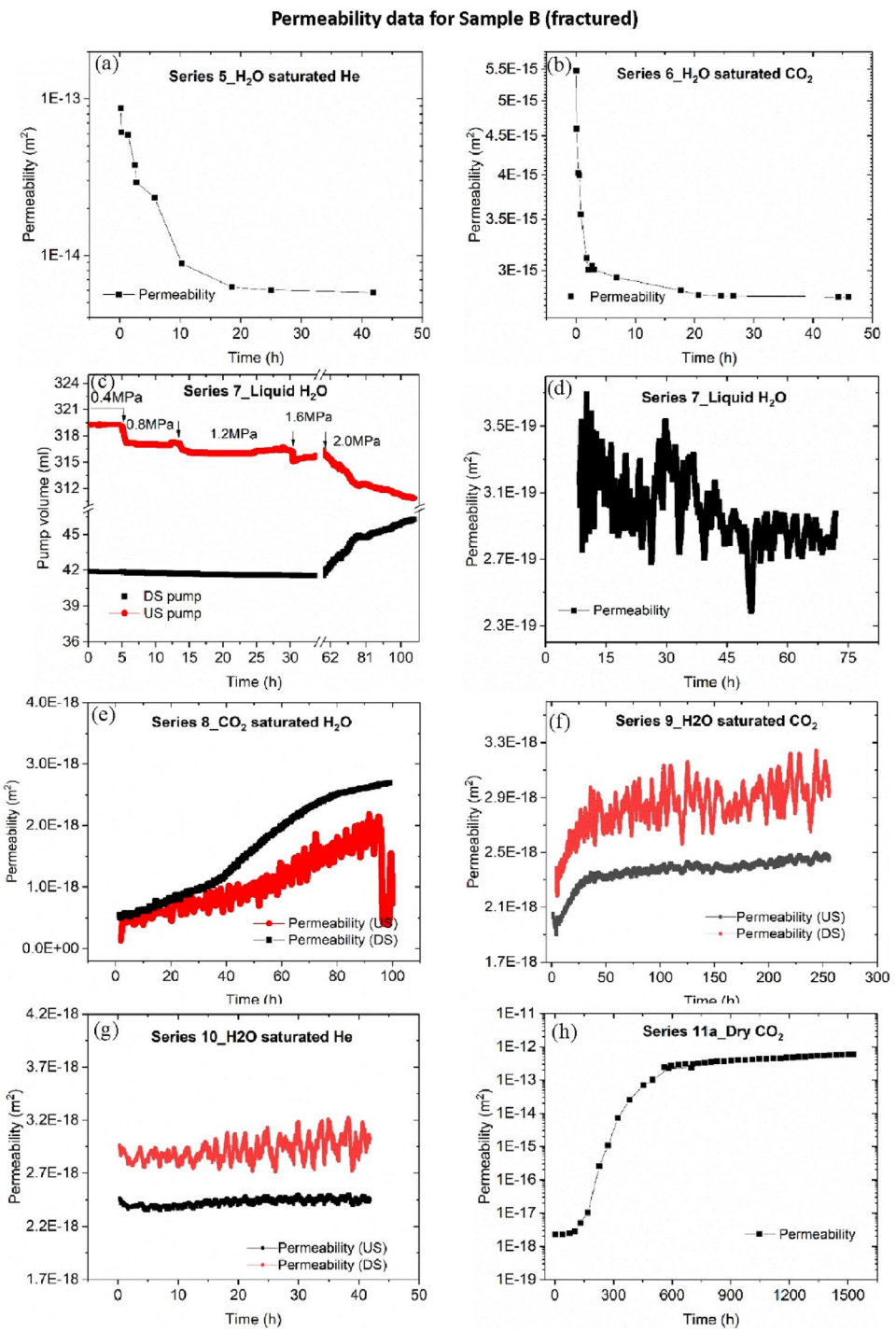

Fig. 5 Permeability data obtained for fractured Sample B (bedding-parallel cracking, pre-equilibrated with ~ 75% relative humidity). **a** Permeability change obtained in Series 5 measurements using water-saturated He. Mean permeability of 10 runs versus elapsed experimental time. **b** Mean permeability measured in all 13 runs performed using water saturated CO_2 (Series 6), plotted against elapsed experimental time. **c** Differential pressure and pump volume data measured in Series 7 (1 run) performed using liquid water. **d** Permeability versus flow time data measured in Series 3 using liquid water. **e** Permeability versus flow time data measured in Series 8 test (1 run) using CO_2 saturated water. **f** Permeability versus flow time data measured using water saturated CO_2 (Series 9, 2 run). **g** Permeability versus flow time data measured using water saturated He (Series 10, 1 run). **h** Mean permeability measured in all 47 runs performed using dry CO_2 versus elapsed experimental time (Series 11a)

while being flushed with CO_2, falling from 9.5×10^{-15} to $7 \times 10^{-15} m^2$ after1400 minutes exposure, asymptotically approaching the later value after ~ 400 min. Flushing with 100% H_2O-saturated CO_2, in Runs 1 and 2 of the Series 3 tests, continuously reduced the apparent permeability by more than one order over 470 min, from 6.5×10^{-15} to $3 \times 10^{-16} m^2$ (Fig. 6b, c). Switch to flow of wet CO_2 with 25% H_2O saturation (Series 3, Run 3, Fig. 6d), caused an increase in permeability, from 3×10^{-16} to $5 \times 10^{-16} m^2$ over 1200 min. Representative data obtained in subsequent runs using an alternating wet and dry CO_2 are plotted in Fig. 6e–g, in terms of permeability versus flow time of each run. Generally, the permeability of the gouge layer fell to ~ $3 \times 10^{-17} m^2$ using 100% water-saturated CO_2 as the flowing fluid, and increased to ~ $1 \times 10^{-15} m^2$ during dry CO_2 flow. This permeability change was reversible. However,

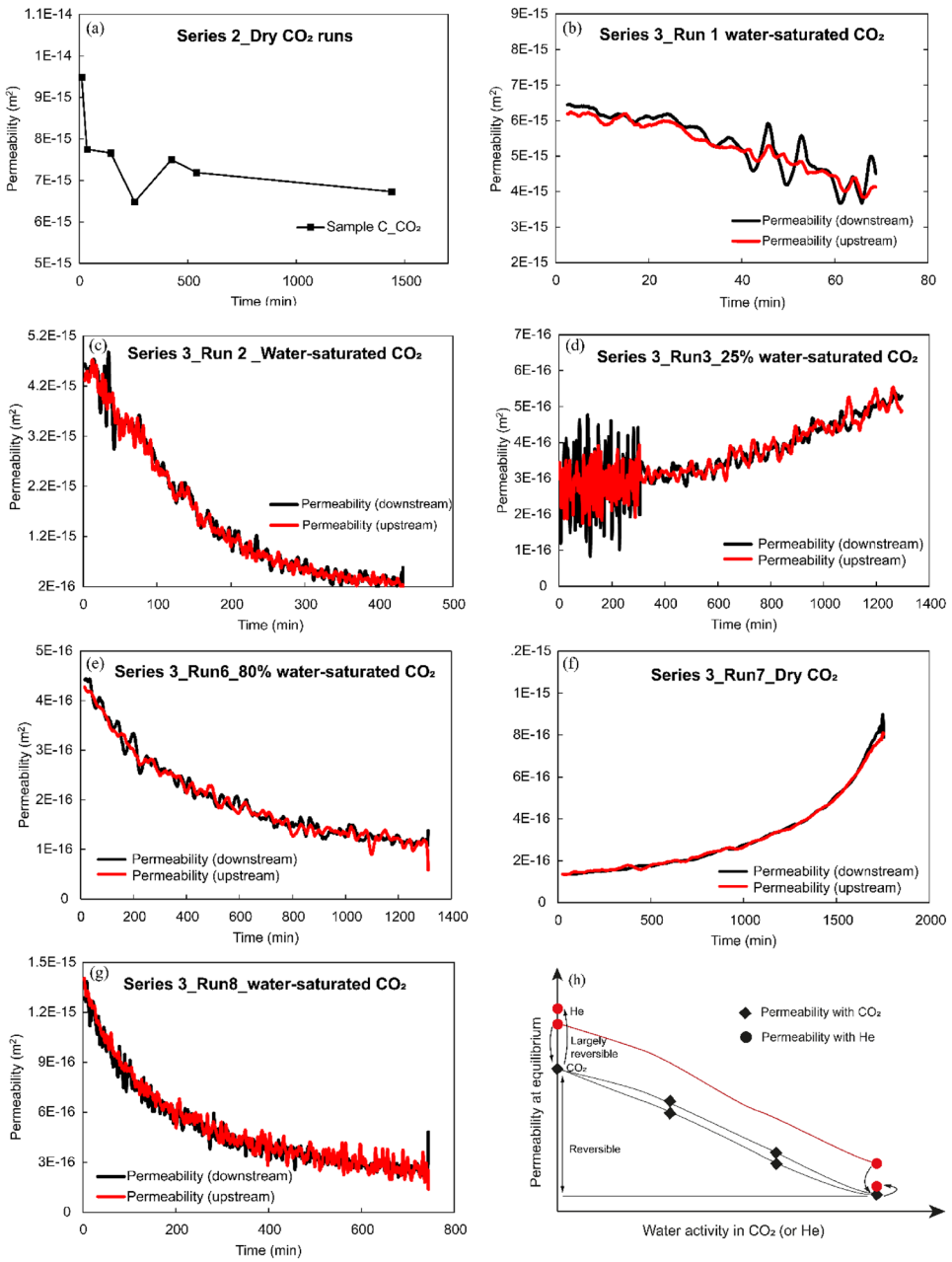

Fig. 6 The (measured) apparent permeability versus flow-through time for Sample C (simulated smectite fault gouge). **a** Permeability evolution over Series 2 runs using (dry) CO_2. Mean permeability values measured for 7 runs are plotted against the elapsed time. **b** Permeability versus flow time data measured in Run 1 using water-saturated CO_2. **c** Permeability versus flow time data measured in Run 2 using water-saturated CO_2. **d** Permeability data measured in Run 3 using 25% water saturated CO_2. **e** Permeability data measured in Run 6 using 80% water-saturated CO_2. **f** Permeability data measured in Run 7 using dry CO_2. **g** Permeability data measured in Run 8 using water-saturated CO_2. **h** Summary of changes in permeability of the clayey sample upon exposure to (dry and variably wet) He and CO_2

whereas the permeability fell rapidly to ~ 3×10^{-17} m^2 when water-saturated CO_2 was introduced and flowed through the sample (over ~ 500 to 1500 min), reversion to ~ 10^{-15} m^2 took much longer (> 5000 min) when dry CO_2 was injected. Note that Run 6 of Series 3, which was performed with 80% water-saturated CO_2, showed a similar permeability to runs performed using fully water-saturated CO_2.

3.2 XRD/IR Data and Sample Scale Observations

Our XRD results (see Appendix 2) on the mineralogical constituents of the OPA and Na-SWy-1 starting material and the three samples (A, B, C) subjected to through-flow experiments are summarized in Table 3. The XRD results show (1) Sample A exhibited a 5% decrease in calcite (21% versus 26% in the OPA starting material) and contained 5% feldspar and 2% siderite, which were not detected in reference OPA material. (2) Sample B exhibited a 11% decrease in calcite content as compared to the reference OPA material. In addition, 3% feldspar and 3% gypsum were detected in Sample B, but not in the reference OPA material. Other mineral components did not exhibit discernible changes above resolution (≥ 3%) in either Sample A or Sample B, relative to the reference material. (3) No detectable change in mineral composition occurred in the simulated smectite gouge (Sample C), in comparison to the reference Na-SWy-1

Table 3 Mineralogical composition of the three samples and reference materials obtained from XRD

Sample ID	Quartz	Smectite	Calcite	Chlorite	Kaolinite	Illite	Feldspar	Gypsum	Pyrite	Siderite	Illi/smec*
OPA reference material	23%		26%	13.16%	4.23%	5.17%			4%		24.%
OPA-Sample A	23%		21%	12%	6%	6%	5%		3%	2%	22%
OPA-Sample B	24%		15%	14.5%	4.5%	7.5%	3%	3%	4%	2%	22.5%
Na-SWy-1_Raw	7%	76%	–	–		–	15%		–		
SWy-1_Sample C	10%	74%	–	–		–	14%		–		

*Mixed layer of illite and smectite with smectite accounting for ~ 20%

montmorillonite. Change in sample mass was also trivial. Similarly, the results of Infrared analysis on Sample C versus the reference Na-SWy-1 clay suggest no new bond formation in Sample C after testing using variably wet CO_2, which confirms the XRD analysis.

Inspection of Samples A, B and C before and after termination of the flow-through experiments and re/dehydration stages (Sample B) showed no changes in morphology of the samples ends, except in the core of OPA Sample B (cored parallel to bedding). Figure 7 shows photographs taken of the same end of Sample B at different stages of our permeability tests. Figure 7a was shot before any flow-through testing, and shows multiple hairline fractures. Figure 7b was shot after experiments on intact Sample B using dry He and dry CO_2 (Series 1–4), showing minor but more prominent fractures. Two main fractures appeared in Sample B when rehydrated to 75% relative humidity after cyclic dehydration and rehydration treatment (Fig. 7c). Figure 7d was taken after the fractured Sample B had undergone all through-flow runs using the full range of

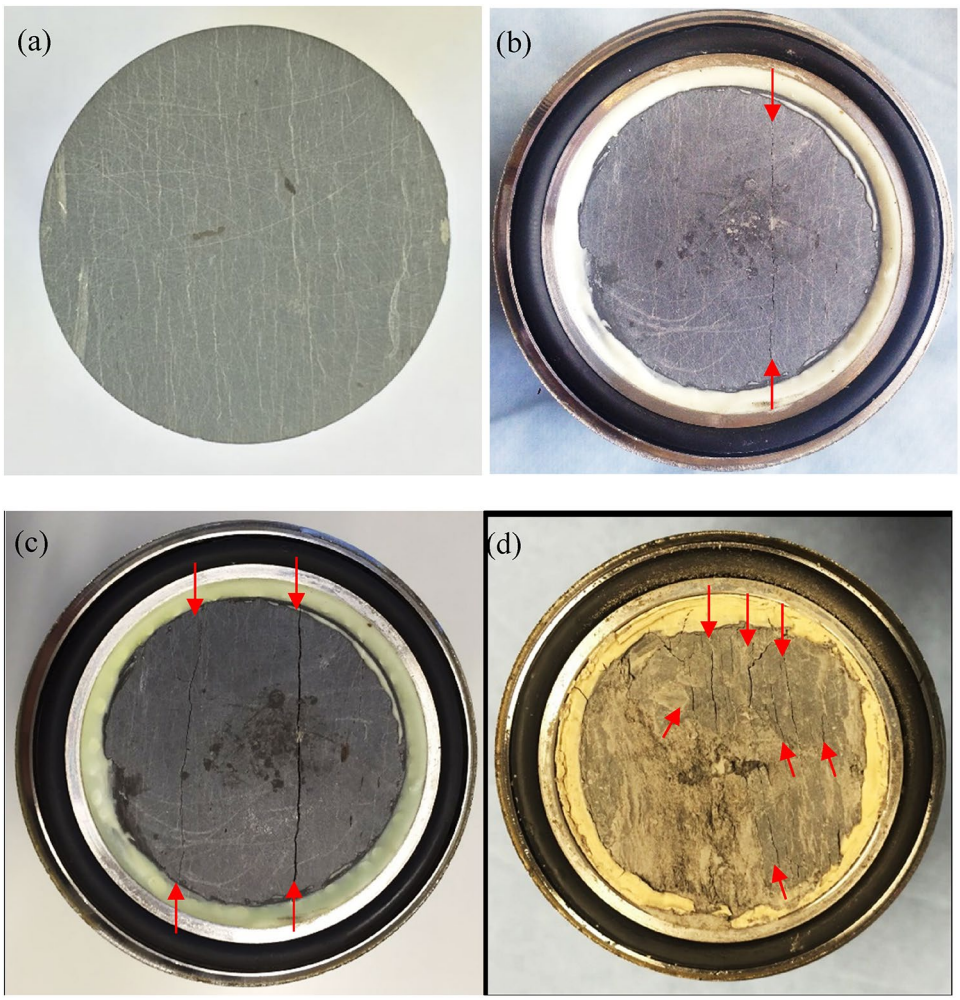

Fig. 7 Photographs of the same end face of Sample B at different stages of our permeability tests. **a** The initial condition before experimentation, with multiple native fractures visible parallel to bedding laminations. **b** Fractures (indicated by red arrow) present after cycles of dry Helium and dry CO_2 flow-through runs (Series 1–4). **c** Two main fractures were present when rehydrated to 75% relative humidity after cyclic dehydration and rehydration treatment. **d** Sample bedding layers split to form well-developed dilatant fractures after through-flow runs sequentially using a variety of pore fluids (i.e., after Series 6–11 runs)

flowing fluids employed, and shows well-developed fractures and delaminated bedding.

4 Discussion

The permeability experiments performed in the present study were mainly aimed at investigating how the previously reported swelling/shrinkage behaviour of smectite due to interaction with CO_2 and water would affect the permeability of smectite-bearing claystone and simulated smectite-rich fault gouges under laterally-constrained displacement boundary conditions. The intention was to provide constraints for evaluating the sealing integrity of fractured and faulted clay-rich caprocks overlying CO_2 storage reservoirs, where swelling/shrinkage effects in open fracture walls and dilated gouge-filled faults may cause large transmissivity changes under laterally constrained subsurface conditions. In the following, we will discuss our results and attempt to explain the phenomenological trends observed.

4.1 Behaviour of the OPA Claystone Samples

4.1.1 Imposed Boundary Conditions

The two Opalinus Clays samples tested in the present study (Samples A and B) were glued into the permeametry vessel, creating a zero lateral strain and zero initial radial stress condition prior to pore fluid pressure introduction. Upon introduction and equilibration of 10 MPa fluid pressure, the stainless steel sample vessel inevitably expanded by a small amount, which means the samples would experience small (effective) tensile stresses caused by elastic vessel expansion plus the effects of poroelastic contraction of the sample. Based on the theory of a thin-walled elastic cylinder and assuming a Yong's modulus of 200 GPa, the radial expansion of the stainless-steel sample vessel (i.e., the radial tensile strain of the sample) at 10 MPa mean pore pressure was estimated to be ~ 1×10^{-4}, which represent a negligible change in the intended zero radial strain boundary condition. Such tensile strain corresponds to tensile stresses of 0.1–0.4 MPa, assuming that the 1–4 GPa oedometer Young's modulus (reported by Ferrari et al. 2016) for the Opalinus clay can represent the behaviour of the material in response to stretching deformation. In addition, the sample would be affected by poroelastic effects upon pore fluid pressurization, producing minor contraction, and increasing the aperture of any axial cracks present, so that effective radial stress (i.e., normal/radial confining stress minus pore fluid pressure) remains at zero or near zero. The lateral boundary conditions imposed are thus similar to those experienced by rock matrix located at or close to open fractures or faults present in a caprock unit (e.g., adjacent to a vertically orientated fracture or fault). The displacement and stress boundary conditions employed therefore correspond to more or less the worst-case scenario that might occur in-situ, where fractures and faults in a caprock unit are open and free of effective normal stresses, and hence most likely to allow vertical advective flow and leakage of stored CO_2. In this situation, the effects of clay swelling or shrinkage on fracture or fault aperture and permeability are expected to be greatest.

Another important point is that the slight deviations from the intended conditions of zero radial strain and zero effective radial stress, caused by purely mechanical effects of the pore fluid at fixed mean pressure, would be the same for all fluid compositions used. This means that changes in sample permeability produced by changing fluid composition at a fixed mean pore pressure (10 MPa) can only reflect differences in the effects of interactions between the rock matrix and the pore fluids employed (e.g., swelling/shrinkage due to sorption–desorption effects).

4.1.2 *Effects of Alternating Flow of Dry He and Dry CO_2 on Intact OPA Samples A and B*

4.1.2.1 Permeability Anisotropy to He Versus CO_2 Our permeability experiments on intact OPA Samples A (Series 1) and B (Series 1,3) showed that dry He permeability of Sample A measured perpendicular to bedding ($2.9 \times 10^{-18} m^2$) was more than 3 orders lower than that measured parallel to bedding using Sample B ($5 \times 10^{-15} m^2$) (see Table 2, Fig. 3a, c, Fig. 4a, e). This demonstrates that a strong permeability anisotropy due to the laminated bedding. Through-flow perpendicular to bedding is presumably controlled by transport through sparse, poorly connected pore networks that must traverse the clay-rich sedimentary laminations forming highly tortuous paths. However, flow parallel to bedding (Sample B) would be strongly promoted by (visible) microcracks within the bedding (see Fig. 7a), high layer-parallel connectivity and low tortuosity (Houben et al. 2013, 2014).

The permeability measurements subsequently performed on intact OPA Samples A (Series 2) and B (Series 2 and 4), using dry CO_2, showed lower permeability values than measured using He (Figs. 3b, d; 4d, f). Due to its inert and non-adsorbing properties (Giesting et al. 2012a), the He permeabilities are commonly used to characterize the intrinsic transport properties of the rock samples (e.g., Al Ismail et al. 2014). Therefore, the clear permeability reduction effect of dry CO_2 as composed to He, provides strong evidence for an impact of CO_2-rock interactions/reactions, in excess of the poromechanical effect as characterized by He tests. However, the degree of permeability anisotropy was reduced after exposure to CO_2. The CO_2 permeability of Sample A (perpendicular to bedding) was reduced by a factor of ~ 3 relative to the He permeability, whereas the CO_2 permeability of Sample B (parallel to bedding) decreased by a full

order. The most obvious interpretation is that anisotropic swelling occurred preferentially in and normal to the clay-rich sedimentary laminations upon exposure to and uptake of CO_2. This speculation is supported by (a) the anisotropic swelling properties of the OPA claystone upon uptake of water, where the swelling strain perpendicular to bedding 10 times greater than that parallel to bedding (Thury 2002) and (b) the fabric normal swelling effect seen in smectite and illite clays upon exposure to dry CO_2 reported by Zhang et al. (2018) and Zhang (2019). In addition, the permeability of Sample A (flow normal to bedding) decreased immediately when flushed with CO_2 after Helium, and initially showed no dependence on CO_2 flow duration (Fig. 3b, d). By contrast, while the permeability of Sample B (parallel to bedding) to He was independent of flow time (Fig. 4a), the permeability during subsequent CO_2 flow decreased by a factor of ~ 2 in the first 10 h of flow, to a stable value of 4×10^{-16} m^2 (Series 2, Fig. 4d) or 2×10^{-15} m^2 (Series 4, Fig. 4f). This time dependent evolution of permeability seen in intact Sample B clearly demonstrates time-dependent self-sealing. Again this point to CO_2 uptake-induced swelling of the smectite present in the clay-rich laminations in the sample (Giesting et al. 2012b), with the rate of permeability reduction likely being controlled by the rate of CO_2 penetration into the clay layers or by the rate of CO_2 uptake by the smectite constituents (Zhang 2019; Zhang et al. 2022).

Exploring this hypothesis further, dry OPA Claystone has a mean smectite content of ~ 5% (24% illite/smectite mixed layer with a mixing ratio of 4:1, see Table 2). Previous work has shown that smectites with an initial hydration state of H < 1W (e.g., Na-type smectite) or 1W < H < 2W (c.f. Ca-type smectite), swell when exposed to dry CO_2 (Giesting et al. 2012a, 2012b; Zhang et al. 2018). It can also be inferred from previous research (Ferrage et al. 2007b; Zhang et al. 2018) that the smectite component of Samples A and B, which were pre-equilibrated with lab air humidity at 40 °C and then subjected to brief degassing in vacuum before testing pore fluid introduction, would retain these initial hydration states and be capable of taking up CO_2 into the interlayer structure and thus swelling (de Jong et al. 2014). In addition, Zhang (2019) observed that illite and illite-like clays pre-equilibrated with lab air humidity at 40 °C are also able to swell by up to 30% of the swelling strain shown by smectite, upon exposure to CO_2 pressure at 10 MPa. Hence, the present results on permeability change and anisotropy for OPA samples strongly suggest a self-sealing effect caused by CO_2 interaction with the smectite and illite content present in the samples investigated.

Of course, other effects might also play a role, such as chemical reaction between components of OPA clay and CO_2, or the Klinkenberg effect due to different pathways or migration mechanism of CO_2 versus He. The possibility of a sealing effect of chemical reactions can be excluded by the fact that XRD measurement on OPA Sample A did not detect changes in the mineral composition in excess of the mineralogical variation, seen in the reference OPA material. Slip flow, such as the Klinkenberg effect, is also unlikely to have contributed to the differences in permeability values between CO_2 and He, since the He and CO_2 fluids at 10 MPa have mean free paths values of ~ 2 nm and ~ 2Å respectively, which are much less than the diameter of the connected pores contributing to the measured permeabilities of > $10^{-19}$$m^2$.

4.1.2.2 Permeability Evolution in Intact Sample B

To examine the effects of repeated alternations in through-flow of dry He versus CO_2, we plotted all permeability versus elapsed time data obtained in the Series 1–4 runs performed on intact Sample B—see Fig. 8. Notably, while the (stable) permeability measured using dry CO_2 is always lower than

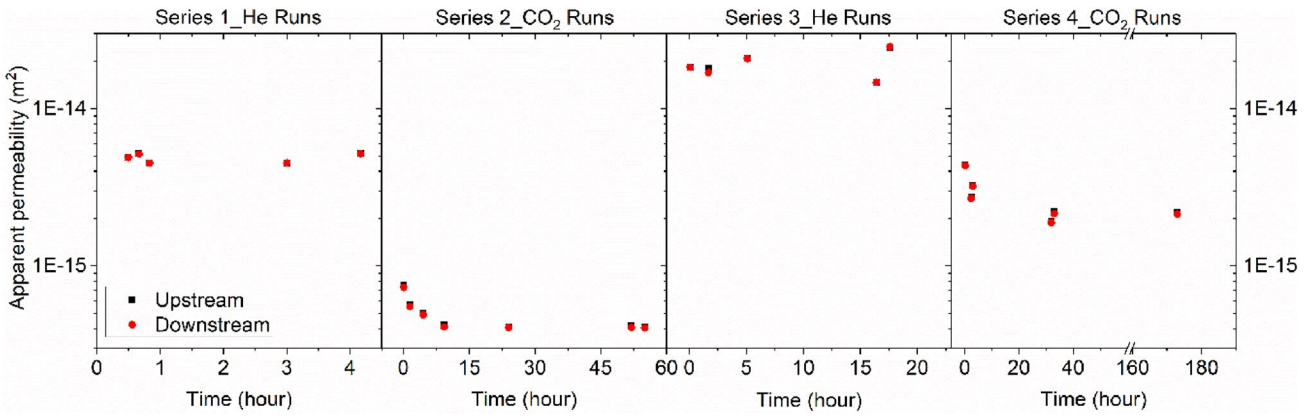

Fig. 8 Evolution of permeability of Sample B during the Series 1–4 through-flow runs performed using dry He and dry CO_2 in alternation. Individual data points respresent the mean permeability of each run plotted versus the corresponding time elasped since pressurization with each fluid shown

measured using dry He (cf. Series 2 versus Series 1 runs and Series 4 versus Series 3 runs in Fig. 8), the decrease in permeability observed upon through flow of dry CO_2 to displace He can be reversed when re-introducing He as flowing fluid to displace CO_2, which demonstrates that the observed permeability changes are due to reversible sorption/desorption effects with CO_2 (superimposed on poro-elastic effects quantified using dry Helium). Besides, permeability values to He and to CO_2 increased after the first series of CO_2 runs (i.e., after the Series 2 runs). Our interpretation is that cyclic pressurizing and depressurizing created through-going fractures or widened existing fractures, as evidenced by those observed at the end of the sample after the Series 1–4 experiment (Fig. 8b). Specifically, we infer that initial replacement of He (Series 1) with CO_2 (Series 2) led to intercalation of CO_2 into the interlayer structure of the smectite phase, while H_2O migrated from the interlayer into the free CO_2 fluid, yielding an overall swelling effect and crack permeability reduction. The swelling effect contributed by CO_2 intercalation (Series 2) was then reversed when the CO_2 fluid was displaced by He (Series 3), and along with flushing out of the water molecules dissolved in the CO_2 fluid, resulting in a larger net shrinkage and higher than initial permeability. This kind of water-displacement-induced shrinkage of smectite is a typical effect of CO_2 due to partitioning of CO_2 and H_2O between the interlayer structure of smectite and the free CO_2 phase, while He and N_2 reportedly had no such effect (Ilton et al. 2012; Schaef et al. 2012). Final replacement of He (Series 3) with CO_2 (Series 4) ultimately led to CO_2 intercalation in the now drier smectite phase, causing similar swelling and crack permeability reduction (Fig. 8). Note that the He and CO_2 permeabilities measured in the second cycle (Series 3 and 4) are higher than those measured in the first cycle (Series 1 and 2), which is also presumably caused by shrinkage related to loss of water dissolved in CO_2 fluid when displacing CO_2 by He (Series 3).

Galán and Aparicio (2014) found that interaction of saponite (Mg-smectite) with CO_2 leads to decomposition of saponite and precipitation of dolomite. However, our XRD analysis on the gouge or OPA material tested using dry and wet CO_2 did not show formation of carbonate or decomposition of the montmorillonite sample. Thus, we infer that the increase in permeability caused by sequential flow of dry CO_2 and He is related specifically to desiccation fractures induced by progressive net shrinkage of smectite-rich laminations in the rock matix.

4.1.3 Permeability Evolution in Fractured OPA Sample B

4.1.3.1 Effect of Wet He Versus Wet CO_2 –Series 5 Versus Series 6 Runs Following cyclic desiccation and fracturing, OPA Sample B was equilibrated with 75% RH, which means that the main smectite components present in the sample should have assumed a hydration state of ~ 2W (Morodome 2011; Morodome and Kawamura 2009), prior to subsequent permeability testing using wet He (Series 5) and wet CO_2 (Series 6). In the Series 5 runs, exposure to and flow of water-saturated He (RH = 100%) rapidly reduced the permeability of fractured Sample B from 8.6×10^{-14} to 5.8×10^{-15} m^2, with no further change beyond 20 h (Fig. 5a). Smectite swelling due to uptake of and equilibration with water carried by the wet He fluid is believed to be the main reason for the observed permeability reduction. This is supported by the fact that smectite in the 2W hydration state tends to hydrate towards the 3W state upon exposure to RH = 100%, exhibiting crystallite swelling normal to (001) of up to 20% at equilibrium (Ferrage et al. 2010; Morodome and Kawamura 2009).

The equilibrium permeability value reached in the Series 5 runs was further reduced by introduction and flow of H_2O-saturated CO_2 in Series 6, decreasing from 5.5×10^{-15} to 3×10^{-15} m^2 in ~ 3 h, gradually reaching a new steady value of 2.8×10^{-15} m^2 at ~ 20 h (Fig. 5b), which is 1/2 the steady permeability obtained with H_2O-saturated He. Two mechanisms might be responsible: (1) water-saturated CO_2 caused crystallite swelling of the smectite present (H ≤ 3W, pre-equilibrated with RH = 100%), due to (re)partitioning of water and CO_2 molecules in the interlayer structure (Schaef et al. 2012, 2015); (2) water condensation and formation of water films on mineral grain surfaces occurred (Ferrage et al. 2005), due to the fact that the solubility of H_2O in $ScCO_2$ is about 2–3 times of that in He (c.f. Chapoy et al. 2004; Spycher et al. 2003).

4.1.3.2 Effect of Water Versus Water-Saturated CO_2 (Series 7 Versus Series 6) In case of the Series 7 runs, when wet-CO_2 (Series 6) was replaced by water (Series 7), the permeability of fractured Sample B decreased sharply. Near zero flow was measured until a differential pressure of 2 MPa was applied (Fig. 5c). We infer that this 2 MPa differential pressure roughly represents the layer parallel breakthrough pressure of the Claystone investigated (Song and Zhang 2013; Wollenweber et al. 2010). The apparent permeability values measured after breakthrough using water was around $2.9\times10^{-19}m^2$ (Fig. 5d), which is ~ 3 orders lower than measured at equilibrium with water saturated He and water-saturated CO_2 (Fig. 5b, c). The observed reduction in apparent water permeability of Sample B could be due to (a) Formation of condensed water in films on mineral surfaces and in inter-granular pores (Homola et al., 1989, Faulkner and Rutter 2000, Faulkner and Rutter 2003, Moore and Lockner 2004) (b) Smectite particle dispersion and electro-kinetic effects in presence of liquid water (Weber and Stanjek, 2011; Espinoza and Santamarina 2017), or (c) water-induced weakening of the clay matrix combined with constrained swelling-induced compaction driven by swell-

ing stress/pressure (Massat et al. 2016; Wang et al. 2014). These mechanisms can all result in clogging or narrowing of the flow paths available in the proceeding tests.

4.1.3.3 Effect of CO_2-Saturated Water (Series 8) The permeability measured immediately after through-flow of CO_2-saturated H_2O (Series 8), following liquid H_2O flow (Series 7), is similar to that measured with liquid water ($\sim 3\times10^{-18}$ m^2). However, unlike the steady permeability measured with liquid water beyond 50 h of flow, ongoing flow of CO_2-saturated H_2O increased the permeability from 3×10^{-19} to 2×10^{-18} m^2 over 100 h (Fig. 5e). On the basis of the XRD measurements which show that the calcite content of Sample B after experimentation was 11% lower than the reference OPA material, we suggest that this increase was caused by dissolution and removal of carbonates in the through-flowing CO_2-saturated water.

Summary of permeability evolution of (fractured) Sample B.

Above all, several typical permeability responses are observed for Sample B when it is equilibrated with variable flowing fluids applied, the trends are schematically summarized in Fig. 6h. Specifically, (1) exposure to dry CO_2 results in a decrease in permeability of less than 1 order of magnitude as compared to permeability measured with dry He, and such change is largely reversible, reflecting sorption/desorption effects with CO_2 (superimposed on poro-elastic effects quantified using dry Helium). (2) Cyclic introduction of dry CO_2 and dry He measures slight unrecoverable change in permeability (e.g., Fig. 8), presumably due to loss of water molecule adsorbed in the rock matrix and associated desiccation-shrinkage effects. (3) Equilibrium permeability reached with water-saturated CO_2 is about half of that with water-saturated He upon displacement of water-saturated He by water-saturated CO_2, while no significant change in permeability is observed while the sample equilibrated with water-saturated CO_2 is flushed by water-saturated He. We deem that the effect of flowing fluid alternation is related to the higher solubility of water in CO_2 than in He, which causes different re-partitioning of water and CO_2 molecules sorbed by the clay matrix during pore fluid displacement sequences; In contrast to trend (1), it also suggests that the initial water activity with which the sample has equilibrated takes an effect. (4) The equilibrium permeability measured with wetter CO_2 are significantly lower than that measured with dry CO_2, demonstrating that the water activity in CO_2 plays a critical role in controlling change in permeability.

4.2 Behaviour of Simulated Smectite Faults Gouge (Sample C)

Gouge-filled faults are more likely to present leakage pathway compared to intact caprock (Frash et al. 2017; Bakker 2017; Song and Zhang 2013). The present experiments on Sample C addressed a simulated smectite gouge layer subjected to boundary conditions mimicking the in-situ condition of an initially dilated and transmissive fault gouge, i.e., near zero lateral strain with low effective normal stress acting on the fault. We chose Na-SWy-1 montmorillonite "gouge" because fault gouges in clay-rich rocks are frequently enriched in smectite compared to the wall rock (Chen et al. 2012).

Our results for this gouge, with its initial hydration state of H < 1W, show that exposure to and subsequent flow-through of dry He (Series 1) and then dry CO_2 (Series 2) causes a decrease in apparent permeability from $5\times10^{-14}m^2$ using He to $7\times10^{-15}m^2$ using CO_2 (Fig. 6a). CO_2-mineral reactions are excluded by the XRD and FTIR results, which showed no changes in the final versus initial mineralogy of Sample C. This is in agreement with research by Krukowski et al. (2015) that recorded no carbonate mineral formation in Na-exchanged montmorillonite (Na-STx-1) after being charged with CO_2 up to 6 MPa pressure at 35 and 50 °C. Given the inferred initial hydration state of Sample C (< 1W), the decrease in permeability measured for dry CO_2 flow versus dry He must then reflect the swelling effect caused by CO_2 uptake or sorption into the smectite interlayer, as reported by Giesting et al. (2012b) and (Rother et al. 2013).

In addition, subsequent flow-through runs (Series 3) performed sequentially using variably wet CO_2 and (pure) dry CO_2 showed that flow of water-saturated CO_2 was able to reduce the permeability of the dry clay gouge by ~ 2 to 3 orders (Fig. 6b–c), and that such reduction could be reversed by continuous flow of CO_2 with lower H_2O content (Fig. 6b–c). These trends are similar to those observed in our experiments on fractured Sample B (Fig. 6h) and indicate that (1) shrinkage/swelling effect resulting from clay interactions with CO_2 and/or water leads to largely reversible changes in permeability, given sufficient time for equilibration, which in turn confirms that the observed permeability changes are due to sorption/desorption effects. (2) The dominant effect controlling permeability is the swelling/shrinkage effect of water uptake and removal, with interlayer CO_2 uptake and other interactions playing a relatively minor role in wet systems.

5 Implications

We now explore the implications of our results for reservoir behaviour and especially for the sealing integrity of fractured and faulted clay-rich caprocks in the context of both CO_2 storage and CO_2-enhanced oil/gas recovery.

5.1 *Effect of CO_2 Injection on Sealing Efficiency of Clay-Rich Caprock and Fault Systems*

During charging of subsurface CO_2 storage systems, such as depleted gas/oil reservoirs or saline aquifers, large amounts of (supercritical) CO_2 will be injected into the storage reservoir at a relatively high rate (million of tons per year, Esposito et al. 2011). The CO_2 injected is anhydrous or of low water content, to reduce corrosion effects occurring in the steel pipelines and other infrastructure during surface transportation (Doctor et al. 2005). During the injection stage, a region of anhydrous supercritical CO_2 will form immediately around the wellbore as the pore fluid (brine) present in affected region of reservoir formation is displaced. The dry CO_2 region is to be surrounded by a wet CO_2 region. Beyond that, brine containing dissolved and capillary trapped CO_2 will be the dominant fluid phase. Continuous injection will expand the region of anhydrous CO_2 by pushing the CO_2/brine interface into the reservoir formation (Pruess and Muller 2009; Kim and Hosseini 2014; Han et al. 2012).

Against this background, our experimental results have implications for the behaviour of both the reservoir and caprock systems when these are clay rich show that the permeability coefficient of clay-rich OPA sample (Sample B) measured using water saturated CO_2 is considerably higher than that measured with liquid water and CO_2 saturated water. Moreover, flow of drier CO_2 through the clay-rich sample pre-equilibrated to high water activity (i.e., liquid water) results in tremendous increase in permeability due to desiccation and associated shrinkage effect, might be sufficient to cause propagation of desiccation effect into the caprock, thereby our result mean that migration/flow of the latterly inject CO_2 should become easier in the reservoir formations where the before-injected CO_2 phase has displaced existing brines, and with continuous flow of dry CO_2 alongside with proceeding of the desiccation-induced permeability increment, the injection might be greatly facilitated.

Applying these implications to clay-rich caprocks near the CO_2 injection well, the risk of caprock leakage related to desiccation induced cracks must be considered. Cracks initiated due to dry CO_2 flow in the reservoir or at the base of the caprock will probably propagate upward, especially near the wellbore during continuous injection of anhydrous CO_2, potentially creating pathways for convective flow of dry CO_2 in the caprock. As demonstrated in the present study, dry CO_2 flow is able to increase the permeability of wet clay-rich materials, possibly leading to a self-enhancing feedback loop, finally resulting in resulting in leakage pathways extending through (Espinoza et al. 2015). Fortunately, a detrimental feedback loop of this kind can be prevented through proper regulation of the injection rate (Song and Zhang 2013). Nonetheless, the limiting injection rate has to be investigated with consideration for specific-site conditions.

During injection of CO_2, the pressures of the pore fluid (CO_2 plume and CO_2 charged brine) within a storage reservoir will be regulated to remain under the capillary entry or breakthrough pressure of the caprock, i.e., the pressure required to displace formation water from pores and conduits in the caprock. For the depleted oil/gas reservoir, which have caprock with proved sealing capacity, CO_2 in the reservoir can only penetrate and migrate within the intact caprock via diffusion, whereas advective flow (Darcy flow) can only occur within locally connected pores and fractures (Song and Zhang 2013). Zhang et al. (2018) demonstrated that introduction of dry CO_2 to room-dry smectite in a closed system will cause swelling (stress) and cause no effect to water- saturated smectite. Present study shows that the impact of CO_2 through-flow on the permeability of a clay-rich shale or simulated gouge strongly depends on water activity in the CO_2 fluid and the proceeding hydration state of the clay component, which in turn refers to activity of water in the initial pore fluid. If the gas/fluid pressure is lower than the sum of reservoir pressure and gas entry pressure, no volumetric or Darcy flow is expected, thus the caprock should function as good seal in terms of capillary sealing mechanism. In the long term, if structure pathways across the caprock are created, e.g., due to activation of faults, the leakage of CO_2 would occur. If the leaking CO_2 is relatively dry (activity of dissolved water < smectite interlayer water activity), then the smectite component of the clay-rich caprock will shrinkage and a self-enhancing feedback loop will be created (c.f Run11 on Sample B, Fig. 5h). On the other hand, if the

CO_2 is relatively wet (activity of dissolved water is larger than smectite interlayer water activity), then no such feedback loop will occur and the fault may even seal (cf. Run 6 on Sample B, Fig. 5b). Note that this is only inferred in consideration of the CO_2-smectite interaction, the other physi-chemical interaction between CO_2 and components of caprocks are not taken into account.

There are very few observations of caprock exposed to CO_2-rich brines. Preliminary examination of core recently recovered from scientific drilling of a natural CO_2 accumulation in Utah suggests that the diffusion of CO_2 into reservoir caprocks drives dissolution of Fe-oxides but subsequent precipitation of carbonate minerals likely retards the diffusion distance of the CO_2 (Kampman 2014). Therefore, the self-enhancing permeability as a result of carbonite dissolution is not likely to happen in the caprock system, where the advective flow of CO_2 charged brines is negligible and that diffusion is the main transport mechanism.

5.2 *Implications for CO_2-EOR and EGR*

In the case of CO_2 storage oil and gas reservoir, first implication discussed in above section applies. In addition, our results have implications for CO_2-enhanced oil/gas recovery. In current industrial production of oil and gas, hydro fracturing operations are conducted using water-based hydraulic fluid to improve recovery rate, especially for unconventional shale gas and oil exploitation (Gandossi 2013; King 2010). However, injective transport of such fluid into gas and oil shales, which is critical for initiation and propagation of fractures, will generally cause spontaneous uptake of the aqueous fracturing or treatment fluids by the clay components in the shale matrix. The associated swelling effect of the smectite component has been reported to result in well-failure and permeability shut-down in the reformed reservoir formation, especially in reservoir systems with high clay content (Anderson et al. 2010). Previous experiments have shown that CO_2-saturated H_2O and H_2O-saturated CO_2 will not lead to swelling effects in smectite material that is pre-equilibrated with liquid water in batch test (Zhang 2019), while the present study demonstrated that (a) convective flow of dry CO_2 through smectite-bearing rock pre-equilibrated with liquid water activity will considerably enhance the permeability through initiation of desiccation-induced fractures or widening of fracture apertures; (b) flow of water-saturated CO_2 through initially water saturated OPA Claystone yield an equivalent or higher permeability than that measured using liquid water. This implies that anhydrous CO_2 has a great potential to be used as an alternative hydro-fracturing fluid for clay-rich reservoir formations, if it can be injected fast enough to avoid hydration. At the stage of hydraulic fracturing stage, large amounts of hydraulic fluid will be injected. In the scenario of CO_2 injection/fracturing, convective flow of anhydrous CO_2 along pre-existing or hydraulically induced fractures is likely to cause shrinkage of the matrix surrounding the fractures, and enhance the permeability through development of desiccation-induced fractures. This will in turn facilitate hydraulic fluid injection, helping avoid injection clogging resulting from fluid uptake by and swelling of clay components in the scenario of water-based hydraulic fluid. In addition, CO_2 at most reservoir P–T conditions is in super critical state, which is miscible to oil and gas, this enables the CO_2 injected to displace the oil/gas trapped in micro-pores through capillary mechanism, hence enhancing the gas/oil recovery rate. However, some operational challenges and difficulties need to be overcome, such as storage and transport of large amount of SC-CO_2 required for fracturing activities at industrial scale, proppant carrying and transport, CO_2 recycling and desiccation (Zhang et al. 2017).

6 Conclusions

We performed permeability experiments on radially constrained Opalinus Claystone cylinders (35 × 70 mm), cored perpendicular (Sample A) and parallel to the bedding (Sample B), at near zero initial radial stress. A similar third sample (Sample C) was investigated, consisting of a simulated smectite gouge layer (Na-SWy-1 montmorillonite) pre-pressed and sandwiched between two stainless steel half-cylinders. Permeability runs using dry He (control experiment) and then dry CO_2 were conducted on all three samples. In addition, Sample B was desiccation-fractured and pre-equilibrated with 75% relative humidity after repeated through-flow runs using dry He and CO_2, and then subjected to multiple series of permeability runs performed using water-saturated He, water-saturated CO_2, liquid H_2O, water-saturated CO_2, water-saturated He, dry CO_2 and dry He. Sample C was tested using alternating flow of variably wet CO_2 and finally dry CO_2. All permeability experiments were done at 40 °C with a mean pore fluid pressure of 10 MPa, except for the last two serial runs on Sample B, which employed variable mean fluid

pressure of dry CO_2 and He. Our main findings can be summarized as follows:

1. Introduction and through-flow of dry CO_2 through room-humidity-equilibrated Opalinus Claystone samples and simulated smectite fault gouge recorded a decrease in stabilized (long term) permeability in all three samples tested, by a factor of 4–9 or even by > 1 order, in comparison to control runs performed using dry He. This confirms a self-sealing effect related to swelling of smectites characterized by a hydration state < 1W prior to exposure to and through-flow of dry CO_2.
2. The permeability of OPA cores showed significant anisotropy in directions perpendicular versus parallel to bedding. The He permeability measured parallel to bedding was more than 3 orders of magnitude higher than perpendicular to bedding, presumably reflecting the different aperture and tortuosity of flow pathways associated with flow parallel to versus perpendicular to bedding. The extent of permeability anisotropy decreased in CO_2 measurements, to less than 3 orders of magnitude, which reflects a different effect of CO_2 on reducing the permeability parallel to and perpendicular to bedding. The most obvious interpretation is that anisotropic swelling occurred preferentially in and normal to clay-rich sedimentary laminations upon exposure to CO_2.
3. Stable (long term) permeability values measured for OPA Sample B (parallel to bedding) using water-saturated CO_2 and then water-saturated He are similar to those measured using CO_2-saturated water. By contrast, large volumes of dry CO_2 flow caused a permeability increase by up to 3 orders in Sample B when pre-equilibrated with liquid water activity, reflecting a desiccation effect of the smectite interlayer and associated shrinkage plus porosity/permeability increase.
4. Stable permeability measured using dry CO_2 for air-dried (H < 1W) simulated smectite fault gouge is ~ 1 order lower than that measured using dry He. Alternating flow of water-saturated CO_2, water-saturated CO_2 and dry CO_2 through the simulated smectite gouge leads to a time dependent change in permeability by 1–2 orders. Such changes in permeability are more or less reversible and caused by uptake/loss of water and/or CO_2 by the smectite components.
5. Whether the permeability in smectite-bearing claystones increases or decreases with continuous flow of CO_2-rich fluid, depends on the water activity to which the sample has been pre-equilibrated versus the water activity in the CO_2 bearing fluid. Water uptake or loss plays the dominate role in controlling change of permeability in smectite-bearing claystone, with the CO_2 having an additional minor effect through CO_2-water-smectite interactions
6. Our experimental results have the following implications for CO_2 subsurface storage system sealing by fractured and faulted clay-rich caprocks under the shallow subsurface conditions under (T = 40 °C). (a) CO_2 migration into fractures/faults in smectite-bearing caprocks pre-equilibrated with pore water activity, is likely to cause a self-sealing effect, and reduce leakage potential of pre-existing pathways. The sealing enhancement effect is most significant (i.e., up to 2–3 orders permeability reduction) when a wet CO_2 phase migrates into pre-exisiting cracks in caprocks that are initially equilibrated with a low water activity. (b) Little effect will occur if the water dissolved in CO_2 has similar activity as water present in the interlayer of smectite component of the caprock. (c) However, flow of relatively dry CO_2 (activity of dissolved water < smectite interlayer water activity) will cause shrinkage to the smectite component of fractured/faulted the clay-rich caprock and cause a self-enhancing feedback loop, increasing the (local) permeability by 2–3 orders. In the vicinity of an injection well where a large amount of anhydrous CO_2 is present during injection, such a self-enhancing feedback loop might cause progressive opening extension of pre-existing leakage pathways, hence increasing leakage hazard. This potential leakage risk needs to be further investigated and measures should be taken to avoid it. On the other hand, this type of self-enhancing feedback loop accompanying convective flow of anhydrous CO_2, could facilitate dry CO_2 injection into clay-rich reservoirs. This suggests some potential for using anhydrous CO_2 as a hydraulic fluid to control swelling-related problems in hydraulic fracturing operations in clay-rich oil/gas reservoir formations, which are frequently encountered using water-base hydraulic fluids.

Appendix

Appendix 1. Calibrations and Data Processing

Calibrations

System Leakage Calibration

Before initiating permeability experiments with any given fluid (e.g., CO_2, He, water), the leakage rate of each pump (Pumps I and II) with respect to that fluid was measured. This was done by isolating each pump and associated pipework from the sample and running the pumps in constant pressure mode at 10 MPa and 40 °C for 20–40 h. Linear fits to all pump volume versus time data, obtained for Pumps I and II with respect to CO_2, yielded leak rates of 2.69 and 12.95µL/h, respectively. The best fit leak rates measured with respect to Helium for Pumps I and II were 828.6 and 874.695µL/h, respectively. The liquid water leak rates measured for Pumps I and II were 22.2 and 35µL/h. The data obtained were used to correct all permeability for leakage as a function of time.

System Volume Calibration

The internal volume of the high pressure valves and tubing that connect the ISCO pumps to the sample assembly was measured before samples were subjected to permeability measurement. This was done using a dummy sample assembly consisting of a stainless steel cylinder (35 mm in diameter and 50 mm long). Following installation of the dummy sample assembly in the experimental set-up, the system was evacuated and isolated from the two ISCO pumps (by closing valves A and C, see Fig. 2f). Both pumps were then primed with He at 8 MPa (He bottle pressure) (via valves B and D, Fig. 2f), reisolated and pressurized to and maintained at 10 MPa in pressure control mode. When the pump temperature and volume signals stabilized, the vacuum filled lines to the dummy sample were reopened, and the volume changes measured by the pumps at the new equilibrium state was taken as the US and DS tube volumes.

Benchmarking the Differential Pressure

Benchmark calibration runs were performed to determine the error in pressure difference obtained by subtracting the raw pressure signals measured at the two ISCO pumps. This was done with the two pumps directly connected, by operating one pump in constant pressure mode and the other pump in constant volume mode. The values of pressure measured using the pressure transducer mounted on each pump provided the sought error.

Data Processing

In each experimental run, the pressure difference and volume change versus time data obtained from the ISCO pumps were corrected as above for leakage and benchmark pressure difference. The apparent permeability of the sample, assuming that flow through the sample occurred in a series of steady states, was calculated continuously over a moving time window of 5 to 120 min, using Darcy's law written in the form

$$\kappa_{app} = \mu \frac{Q_S}{A} \frac{L}{\Delta P} \tag{A-1}$$

Here, μ is the dynamic viscosity of the fluid [Pa s], Q_s is the leak-corrected fluid flux traversing 'the rock' sample cross section (i.e., the cross section of the OPA cylinders and of the gouge layer) [$m^3 \cdot s^{-1}$], L and A are the length [m] and cross-sectional area [m^2] of the sample, respectively, and ΔP is the corrected pressure difference across the sample [Pa]. We took the viscosities for He, CO_2 and water at 10 MPa and 40 °C as 20.84 uPa·s, 47.82µPa·s and 653.87µPa·s respectively (http://webbook.nist.gov). Since the mole fraction of H_2O present in H_2O-saturated CO_2 is low (0.0036) at 10 MPa and 40 °C (Duan et al. 2003), we assumed that the viscosity of wet and water-saturated CO_2 at the present experimental P–T conditions is the same as dry CO_2. The viscosities of water-saturated He and CO_2-saturated liquid water were similarly assumed to be the same as pure He and pure liquid H_2O. In calculating κ_{app} from Eq. (1), Q_s was obtained from linear regression fits to our pump volume versus time data using the above-mentioned moving time window of 5 to 120 min duration, depending on flow rate and run duration. The corrected pressure difference ΔP was obtained from the average taken over the same window.

Appendix 2. Representative Results of XDR and Infrared Analysis

Representative XRD profiles measured for the referential OPA material are plotted in Fig. A1, which also shows how the profiles were decomposed to quantitatively determine the mineral composition of the material tested. The results of Infrared analysis on Sample C versus the reference Na-SWy-1 clay are given in Fig. A2.

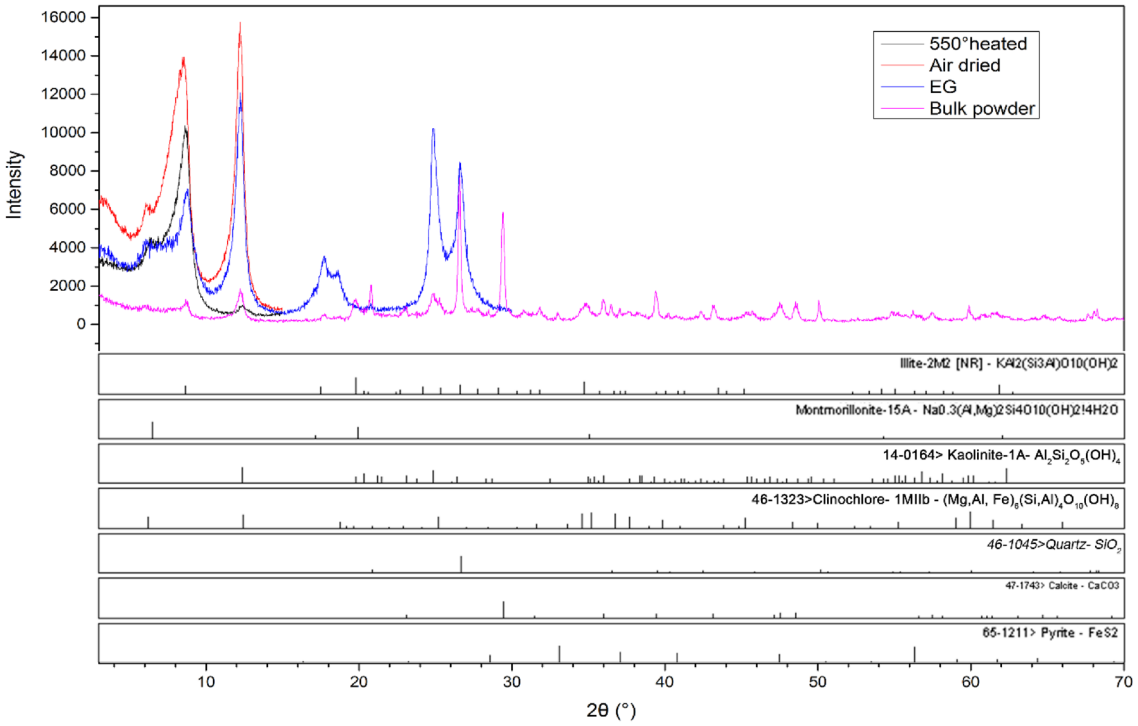

Fig. A1 Representative data collected in XRD measurements on reference OPA material and decomposition of the XRD profiles for quantitative determination of material mineral composition

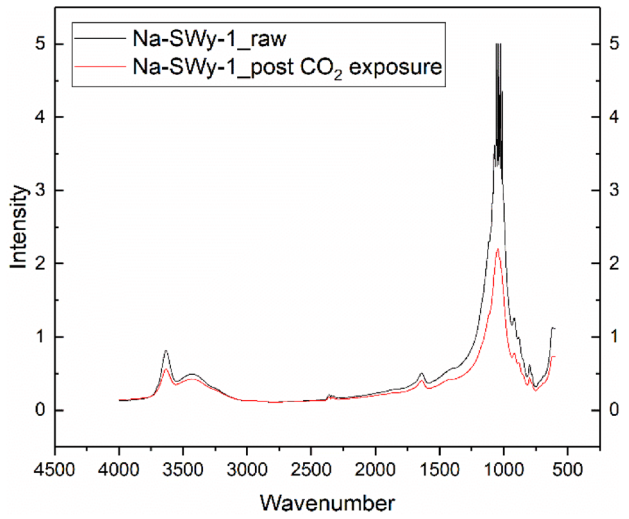

Fig. A2 Infrared spectroscopy obtained for Sample C and reference Na-SWy-1 montmorillonite

Acknowledgements Authors declare that they have no conflict of interest. This study was performed within the Dutch National Carbon Capture and Storage Research Programme (CATO-2) under direct funding by Shell Global Solutions International B.V. The first author Zhang acknowledges China Scholarship Council (CSC) for financial support. We also thank A. Busch, H.M. Wentinck and T.K.T. Wolterbeek for fruitful discussions on the experimental design and associated results.

The authors thank the two anonymous reviewers for many critical comments that helped improve this manuscript.

Data availability Raw data were generated at the High Pressure and Temperature Laboratory, Utrecht University. The authors confirm that the (derived) data supporting the findings of this study are available within the article and its supplementary materials. The raw and derived data are also available from the corresponding author Zhang on request.

References

Akono A-T, Druhan JL, Dávila G, Tsotsis T, Jessen K, Fuchs S, Crandall D, Shi Z, Dalton L, Tkach MK, Goodman AL, Frailey S, Werth CJ (2019) A review of geochemical–mechanical impacts in geological carbon storage reservoirs. Greenhouse Gas Sci Technol 9:474–504

Al Ismail M, Reece J, Hol S, Zoback M, (2014). The Effect of CO_2 Adsorption on Permeability Anisotropy in the Eagle Ford Shale, Unconventional Resources Technology Conference, Denver, Colorado, 25-27 August 2014. Society of Exploration Geophysicists, American Association of Petroleum Geologists, Society of Petroleum Engineers, pp. 1119-1127

Aminu MD, Nabavi SA, Rochelle CA, Manovic V (2017) A review of developments in carbon dioxide storage. Appl Energy 208:1389–1419

Anderson RL, Ratcliffe I, Greenwell HC, Williams PA, Cliffe S, Coveney PV (2010) Clay swelling — A challenge in the oilfield. Earth-Sci Rev 98:201–216

Armitage PJ, Faulkner DR, Worden RH (2013) Caprock Corrosion. Nat Geosci 6:79

Barshad I (1955) Adsorptive and swelling properties of clay-water system. Clays Clay Technol Bull 169:225–238

Benson SM, Cole DR (2008) CO_2 sequestration in deep sedimentary formations. Elements 4:325–331

Berend I, Cases JM, Francois M, Uriot JP, Michot L, Masion A, Thomas F (1995) Mechanism of adsorption and desorption of water-vapor by homoionic montmorillonites. 2. The Li+, Na+, K+, Rb+ and Cs+-exchanged forms. Clays Clay Miner 43:324–336

Bishop JL, Pieters CM, Edwards JO (1994) Infrared spectroscopic analyses on the nature of water in montmorillonite. Clays Clay Miner 42:702–716

Bossart P, Thury M (2008) Characteristics of the Opalinus Clay at Mont Terri. Mont Terri Project, Wabern

Busch A, Alles S, Gensterblum Y, Prinz D, Dewhurst D, Raven M, Stanjek H, Krooss B (2008) Carbon dioxide storage potential of shales. Int J Greenhouse Gas Control 2:297–308

Cases JM, Berend I, Besson G, Francois M, Uriot JP, Thomas F, Poirier JE (1992) Mechanism of adsorption and desorption of water vapor by homoionic montmorillonite. 1. The sodium-exchanged form. Langmuir 8:2730–2739

Cases JM, Berend I, Francois M, Uriot JP, Michot LJ, Thomas F (1997) Mechanism of adsorption and desorption of water vapor by homoionic montmorillonite.3. The Mg2+, Ca2+, Sr2+ and Ba2+ exchanged forms. Clays Clay Miner 45:8–22

Chapoy A, Mohammadi AH, Tohidi B, Richon D (2004) Gas Solubility Measurement and Modeling for the Nitrogen + Water System from 274.18 K to 363.02 K. J Chem Eng Data 49:1110–1115

de Jong SM, Spiers CJ, Busch A (2014) Development of swelling strain in smectite clays through exposure to carbon dioxide. In J Greenhouse Gas Control 24:149–161

Espinoza DN, Santamarina JC (2012) Clay interaction with liquid and supercritical CO2: The relevance of electrical and capillary forces. Int J Greenhouse Gas Control 10:351–362

Espinoza DN, Santamarina JC (2017) CO2 breakthrough—Caprock sealing efficiency and integrity for carbon geological storage. Int J Greenhouse Gas Control 66:218–229

Espinoza DN, Pereira JM, Vandamme M, Dangla P, Vidal-Gilbert S (2015) Desorption-induced shear failure of coal bed seams during gas depletion. Int J Coal Geol 137:142–151

Ferrage E, Lanson B, Malikova N, Plancon A, Sakharov BA, Drits VA (2005) New insights on the distribution of interlayer water in bi-hydrated smectite from X-ray diffraction profile modeling of 00l reflections. Chem Mater 17:3499–3512

Ferrage E, Kirk CA, Cressey G, Cuadros J (2007a) Dehydration of Ca-montmorillonite at the crystal scale. Part I: Struct Evol Am Mineral 92:994–1006

Ferrage E, Lanson B, Sakharov BA, Geoffroy N, Jacquot E, Drits VA (2007b) Investigation of dioctahedral smectite hydration properties by modeling of X-ray diffraction profiles: influence of layer charge and charge location. Am Miner 92:1731–1743

Ferrage E, Lanson B, Michot LJ, Robert J-L (2010) Hydration properties and interlayer organization of water and ions in synthetic Na-smectite with tetrahedral layer charge. Part 1. Results from X-ray diffraction profile modeling. J Phys Chem 114:4515–4526

Ferrari A, Favero V, Laloui L (2016) One-dimensional compression and consolidation of shales. Int J Rock Mech Min Sci 88:286–300

Frash LP, Carey JW, Ickes T, Viswanathan HS (2017) Caprock integrity susceptibility to permeable fracture creation. Int J Greenhouse Gas Control 64:60–72

Galán E, Aparicio P (2014) Experimental study on the role of clays as sealing materials in the geological storage of carbon dioxide. Appl Clay Sci 87:22–27

Gandossi L (2013). An overview of hydraulic fracturing and other formation stimulation technologies for shale gas production. Eur. Commisison Jt. Res. Cent. Tech. Reports

Gaus I (2010) Role and impact of CO2–rock interactions during CO_2 storage in sedimentary rocks. Int J Greenhouse Gas Control 4:73–89

Gaus I, Azaroual M, Czernichowski-Lauriol I (2005) Reactive transport modelling of the impact of CO_2 injection on the clayey cap rock at Sleipner (North Sea). Chem Geol 217:319–337

Giesting P, Guggenheim S, Koster van Groos AF, Busch A (2012a) Interaction of carbon dioxide with Na-exchanged montmorillonite at pressures to 640bars: Implications for CO_2 sequestration. Int J Greenhouse Gas Control 8:73–81

Giesting P, Guggenheim S, Koster van Groos AF, Busch A (2012b) X-ray diffraction study of K- and Ca-exchanged montmorillonites in CO_2 atmospheres. Environ Sci Technol 46:5623–5630

Han WS et al (2012) Modeling of spatiotemporal thermal response to CO_2 injection in saline formations: interpretation for monitoring. Transp Porous Media 93(3):381–399

Heller R, Zoback M (2014) Adsorption of methane and carbon dioxide on gas shale and pure mineral samples. J Unconv Oil Gas Resour 8:14–24

Houben ME, Desbois G, Urai JL (2013) Pore morphology and distribution in the Shaly facies of Opalinus Clay (Mont Terri, Switzerland): Insights from representative 2D BIB–SEM investigations on mm to nm scale. Appl Clay Sci 71:82–97

Houben ME, Desbois G, Urai JL (2014) A comparative study of representative 2D microstructures in Shaly and Sandy facies of Opalinus Clay (Mont Terri, Switzerland) inferred form BIB-SEM and MIP methods. Mar Pet Geol 49:143–161

Ilton ES, Schaef HT, Qafoku O, Rosso KM, Felmy AR (2012) In situ X-ray diffraction study of Na+ saturated montmorillonite exposed to variably wet super critical CO_2. Environ Sci Technol 46:4241–4248

Kaldi J, Daniel R, Tenthorey E, Michael K, Schacht U, Nicol A, Underschultz J, Backe G (2011) Caprock systems for CO_2 geological storage. Cooperative Research Center for Greenhouse Gas Technologies, Canberra

Kaldi J, Daniel R, Tenthorey E, Michael K, Schacht U, Nicol A, Underschultz J, Backe G (2013) Containment of CO_2 in CCS: role of caprocks and faults. Energy Procedia 37:5403–5410

Kampman N, Bickle M, Wigley M, Dubacq B (2014a) Fluid flow and CO_2–fluid–mineral interactions during CO_2-storage in sedimentary basins. Chem Geol 369:22–50

Kampman N, Bickle MJ, Maskell A, Chapman HJ, Evans JP, Purser G, Zhou Z, Schaller MF, Gattacceca JC, Bertier P, Chen F, Turchyn AV, Assayag N, Rochelle C, Ballentine CJ, Busch A (2014b) Drilling and sampling a natural CO_2 reservoir: implications for fluid flow and CO_2-fluid–rock reactions during CO_2 migration through the overburden. Chem Geol 369:51–82

Kim S, Hosseini SA (2014) Above-zone pressure monitoring and geomechanical analyses for a field-scale CO_2 injection project in Cranfield MS. Greenhouse Gas Sci Technol 4(1):81–98

King GE, (2010). Thirty years of gas shale fracturing: What have we learned?, SPE Annual Technical Conference and Exhibition. Society of Petroleum Engineers

Krukowski EG, Goodman A, Rother G, Ilton ES, Guthrie G, Bodnar RJ (2015) FT-IR study of CO2 interaction with Na+ exchanged montmorillonite. Appl Clay Sci 114:61–68

Laird DA (1999) Layer charge influences on the hydration of expandable 2: 1 phyllosilicates. Clays Clay Miner 47:630–636

Loring JS, Schaef HT, Turcu RVF, Thompson CJ, Miller QRS, Martin PF, Hu JZ, Hoyt DW, Qafoku O, Ilton ES, Felmy AR, Rosso KM (2012) In situ molecular spectroscopic evidence for CO_2 intercalation into montmorillonite in supercritical carbon dioxide. Langmuir 28:7125–7128

Loring JS, Ilton ES, Chen J, Thompson CJ, Martin PF, Benezeth P, Rosso KM, Felmy AR, Schaef HT (2014) In situ study of CO_2 and H(2)O partitioning between Na-montmorillonite and variably wet supercritical carbon dioxide. Langmuir 30:6120–6128

Massat L, Cuisinier O, Bihannic I, Claret F, Pelletier M, Masrouri F, Gaboreau S (2016) Swelling pressure development and interaggregate porosity evolution upon hydration of a compacted swelling clay. Appl Clay Sci 124:197–210

Melzer LS (2012) Carbon dioxide enhanced oil recovery (CO2 EOR): factors involved in adding carbon capture, utilization and storage (CCUS) to enhanced oil recovery. Center for Climate and Energy Solutions, Virginia

Middleton RS, Carey JW, Currier RP, Hyman JD, Kang Q, Karra S, Jiménez-Martínez J, Porter ML, Viswanathan HS (2015) Shale gas and non-aqueous fracturing fluids: Opportunities and challenges for supercritical CO_2. Appl Energy 147:500–509

Miocic JM, Gilfillan SM, Roberts JJ, Edlmann K, McDermott CI, Haszeldine RS (2016) Controls on CO 2 storage security in natural reservoirs and implications for CO_2 storage site selection. Int J Greenhouse Gas Control 51:118–125

Morodome S (2011) In situ X-ray diffraction study of the swelling of montmorillonite as affected by exchangeable cations and temperature. Clays Clay Miner 59:165

Morodome S, Kawamura K (2009) Swelling behavior of Na-and Ca-montmorillonite up to 150 C by in situ X-ray diffraction experiments. Clays Clay Miner 57:150–160

Pearson F, Arcos D, Bath A, Boisson J, Fernández A, Gaebler H, Gaucher E, Gautschi A, Griffault L, Hernan P, (2003). Mont Terri Project-Geochemistry of Water in the Opalinus Clay Formation at the Mont Terri Rock Laboratory-Synthesis Report. Federal Office for Water and Geology, FOWG

Rochelle CA, Czernichowski-Lauriol I, Milodowski AE (2004) The impact of chemical reactions on CO_2 storage in geological formations: a brief review. Geol Soc Lond Spec Publ 233:87

Romanov VN (2013) Evidence of irreversible CO_2 intercalation in montmorillonite. Int J Greenhouse Gas Control 14:220–226

Rother G, Ilton ES, Wallacher D, Haubeta T, Schaef HT, Qafoku O, Rosso KM, Felmy AR, Krukowski EG, Stack AG, Grimm N, Bodnar RJ (2013) CO_2 sorption to subsingle hydration layer montmorillonite clay studied by excess sorption and neutron diffraction measurements. Environ Sci Technol 47:205–211

Schaef HT, Ilton ES, Qafoku O, Martin PF, Felmy AR, Rosso KM (2012) In situ XRD study of Ca2+ saturated montmorillonite (STX-1) exposed to anhydrous and wet supercritical carbon dioxide. Int J Greenhouse Gas Control 6:220–229

Schaef HT, Loring JS, Glezakou VA, Miller QRS, Chen J, Owen AT, Lee MS, Ilton ES, Felmy AR, McGrail BP, Thompson CJ (2015) Competitive sorption of CO_2 and H_2O in 2:1 layer phyllosilicates. Geochim Cosmochim Ac 161:248–257

Skurtveit E, Miri R, Hellevang H (2018) Fluid-rock interactions in clay-rich seals geological carbon storage. Wiley, New york, pp 167–185

Song J, Zhang DX (2013) Comprehensive review of caprock-sealing mechanisms for geologic carbon sequestration. Environ Sci Technol 47:9–22

Spycher N, Pruess K, Ennis-King J (2003) CO2-H2O mixtures in the geological sequestration of CO_2. I. Assessment and calculation of mutual solubilities from 12 to 100°C and up to 600 bar. Geochim Cosmochim Ac 67:3015–3031

Thury M (2002) The characteristics of the Opalinus Clay investigated in the Mont Terri underground rock laboratory in Switzerland. Cr Phys 3:923–933

Vinsot A, Appelo CAJ, Lundy M, Wechner S, Cailteau-Fischbach C, de Donato P, Pironon J, Lettry Y, Lerouge C, De Cannière P (2017) Natural gas extraction and artificial gas injection experiments in Opalinus Clay, Mont Terri rock laboratory (Switzerland). Swiss J Geosci 110:375–390

Wang Q, Cui Y-J, Tang AM, Delage P, Gatmiri B, Ye W-M (2014) Long-term effect of water chemistry on the swelling pressure of a bentonite-based material. Appl Clay Sci 87:157–162

Wentinck HM, Busch A (2017) Modelling of CO_2 diffusion and related poro-elastic effects in a smectite-rich cap rock above a reservoir used for CO_2 storage. Geol Soc London Spec Publ 454:155–173

White CM, Strazisar BR, Granite EJ, Hoffman JS, Pennline HW (2003) Separation and capture of CO2 from large stationary sources and sequestration in geological formations—coalbeds and deep saline aquifers. J Air Waste Manag Assoc 53:645–715

Wollenweber J, Alles S, Busch A, Krooss BM, Stanjek H, Littke R (2010) Experimental investigation of the CO_2 sealing efficiency of caprocks. Int J Greenhouse Gas Control 4:231–241

Wolterbeek TKT, Peach CJ, Spiers CJ (2013) Reaction and transport in wellbore interfaces under CO2 storage conditions: Experiments simulating debonded cement–casing interfaces. Int J Greenhouse Gas Control 19:519–529

Wolterbeek TK, Peach CJ, Raoof A, Spiers CJ (2016) Reactive transport of CO2-rich fluids in simulated wellbore interfaces: flow-through experiments on the 1–6 m length scale. Int J Greenhouse Gas Control 54:96–116

Zhang X, Lu Y, Tang J, Zhou Z, Liao Y (2017) Experimental study on fracture initiation and propagation in shale using supercritical carbon dioxide fracturing. Fuel 190:370–378

Zhang M, de Jong S, Spiers CJ, Busch A, Wentinck HM (2018) Swelling stress development in confined smectite clays through exposure to CO2. Int J Greenhouse Gas Control 74:49–61

Zhang M, Spiers CJ, Liu J, Zhou H (2022) Stress-strain-sorption behaviour of smectites upon exposure to dry and wet CO_2. Front Earth Sci. https://doi.org/10.3389/feart.2022.911247

Zhang M (2019). Stress-strain-sorption behaviour and permeability evolution in clay-rich rocks under CO2 storage conditions. UU Dept. of Earth Sciences